

Composite picosecond control of atomic state through a nanofiber interface

Yudi Ma,^{*} Ruijuan Liu, Lingjing Ji, Liyang Qiu, and Saijun Wu[†]

Department of Physics, State Key Laboratory of Surface Physics and Key Laboratory of Micro and Nano Photonic Structures (Ministry of Education), Fudan University, Shanghai 200433, China.

Dianqiang Su and Yanting Zhao[‡]

¹*State Key Laboratory of Quantum Optics and Quantum Optics Devices, Institute of Laser Spectroscopy, Shanxi University, Taiyuan 030006, China.*

²*Collaborative Innovation Center of Extreme Optics, Shanxi University, Taiyuan 030006, China*

Ni Yao and Wei Fang[§]

*Interdisciplinary Center for Quantum Information,
State Key Laboratory of Modern Optical Instrumentation,
College of Optical Science and Engineering, Zhejiang University, Hangzhou 310027, China
(Dated: today)*

Accurate control of single emitters at nanophotonic interfaces may greatly expand the accessible quantum states of coupled optical spins in the confined geometry and to unveil exotic nonlinear quantum optical effects. However, the optical control is challenged by spatially varying light-atom coupling strength generic to nanophotonics. We demonstrate numerically that despite the near-field inhomogeneity, nearly perfect atomic state control can be achieved by exploiting geometric robustness of optical transitions with composite picosecond excitations. Our proposal is followed by a proof-of-principle demonstration where an $N = 3$ composite sequence is applied to robustly invert the D1 population of free-flying ^{85}Rb atoms trespassing a nanofiber interface. The precise control is confirmed by comparing the D2 fiber transmission with full-level simulation of the mesoscopic light-atom interaction across the composite parameter space. We project the scheme to large N for precise phase patterning and arbitrary optical dipole control at the nanophotonic interface.

I. INTRODUCTION

Two-level atoms are ideal nonlinear quantum optical elements featuring large resonant absorption cross-sections combined with single-photon nonlinearity. To arrange 2-level atoms into a useful nonlinear quantum optical network, it is important to mitigate information losses associated with radiation damping. To this end, state-of-art photonic interfaces have been developed to control the spontaneous emission, to support many-body interaction mediated by exchange of confined photons, and for information delivery through well-defined photonic channels into the far field [1]. In particular, it is demonstrated that cold atoms coupled to an optical nanofiber (ONF) [2–6] displays infinitely long-range interaction mediated by exchange of guided photons [7–9]. In this scenario, a potentially paradigm-shifting technique is to precisely control the atomic dipoles with sub-wavelength spatial resolution. Similar to the case of free space control [10, 11], the precise atomic dipolar spin control can be designed to modify the collective coupling strength, to reversibly suppress collective emission into the guided mode on demand, and to access the sub-radiant manifold of collective dipoles [12, 13] featuring

many-body nonlinear quantum optics in the confined geometry [1, 14–23]. However, unlike controlling magnetic spins [24–27] or narrow optical transitions [28–30], optical control of strong transitions with qubit-level precision is itself an outstanding challenge. The technical difficulty is amplified at nanophotonic interfaces where a uniform optical control seems prohibited by a none-uniform light intensity and polarization distribution.

We propose to achieve high precision nanophotonic control of atomic states by implementing a class of composite control schemes [31, 32] with arrays of picosecond pulses [33]. We demonstrate numerically that despite the near-field inhomogeneity, atomic state control with $f > 99\%$ fidelity can be uniformly achieved for confined atoms [3, 34] through evanescent coupling. The projected sub-wavelength scale, nearly perfect atomic state control should therefore open various opportunities in nonlinear quantum optics at the nanophotonic interfaces. Our proposal is followed by a proof-of-principle demonstration where an $N = 3$ composite pulse sequence is applied to robustly invert the D1 population of free-flying ^{85}Rb atoms trespassing an ONF interface.

II. COMPOSITE PICOSECOND CONTROL AT NANOPHOTONIC INTERFACE

Precise control of strong optical transitions can be achieved at a carefully chosen time scale. As the example depicted in Fig. 1d, the optical response of an

^{*} ydma18@fudan.edu.cn

[†] saijunwu@fudan.edu.cn

[‡] zhaoyt@sxu.edu.cn

[§] wfang08@zju.edu.cn

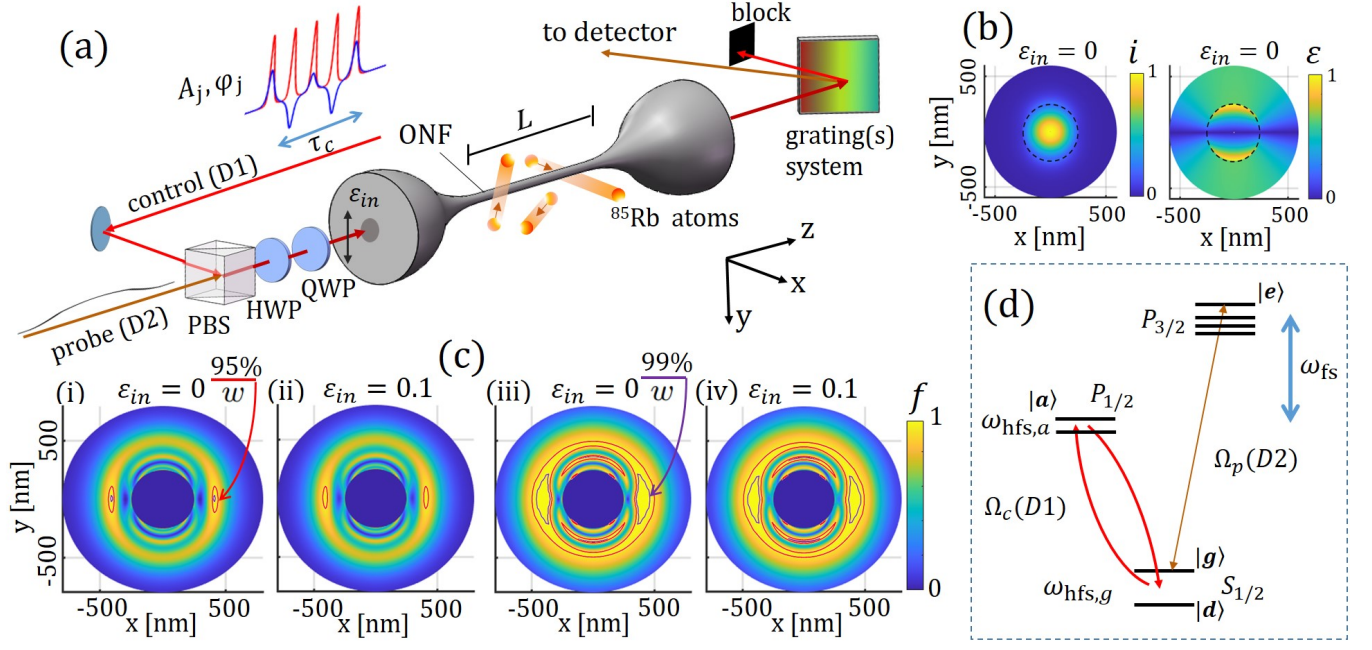


FIG. 1. Schematic setup for composite picosecond control of atomic states through an atom-nanofiber interface. (a): Experimental setup. A picosecond pulse sequence is sent to an optical nanofiber (ONF) to resonantly drive the D1 transition of free ^{85}Rb atoms through the evanescent coupling. The atomic population in the $F = 3$ ground-state hyperfine level ($|g\rangle$) is monitored by a D2 probe. See Fig. (d) on the level diagram. (b): $i(x, y)$ and $\epsilon(x, y)$ distributions near the $d = 500$ nm ONF for the HE_{11}^y -coupled control pulses ($\epsilon_{\text{in}} = 0$, also see Appendix B). The normalized intensity distribution $i(x, y) = |\mathbf{E}(x, y)|^2 / |\mathbf{E}(\mathbf{0})|^2$ decays radially with a characteristic length $\xi \approx 1/\sqrt{\beta_c^2 - k_0^2}$ of 200 nm ($\beta_c \approx 1.2k_0$ is the propagation constant of the HE_{11} mode. $k_0 = 2\pi/795$ nm). The local ellipticity is defined as $\epsilon(x, y) = |\mathbf{E}^* \times \mathbf{E}|/|\mathbf{E}|^2$. For the probe beam in the HE_{11}^y mode, the distributions are similar, but with $x - y$ interchanged. (c): Local population inversion by the highly inhomogeneous HE_{11}^y coupled $N = 1$ (i,ii) and $N = 5$ (iii,iv) control pulses. For stationary atoms, $f = \rho_{aa}(\tau_c) > 99\%$ efficiency can be achieved by optimizing the relative phases $\{\varphi_j\}$ of the composite pulse. See the $f = 95\%$ (red curves), $f = 99\%$ (purple curves, with $w \approx 110$ nm width) contours in the Fig. (c,iii) simulation, with $\{\varphi_j\} = \{0, 5\pi/6, 2\pi/6, 5\pi/6, 0\}$ according to ref. [31]. The efficient inversion is also robust against small incident ellipticity ϵ_{in} (Fig. (c,iv)). For comparison, for the single pulse “ π ” excitation, even the $f = 95\%$ contour is limited to a $w \approx 40$ nm width. The $f = 99\%$ contour is hardly visible in Fig. (c,i), which completely vanishes at $\epsilon_{\text{in}} = 0.1$ in Fig. (c,ii). In Fig. (a) the red (blue) line stands for the intensity (in-phase field quadrature) of the composite pulse envelop. ONF: Optical nanofiber. HWP: half-wave plate. QWP: quarter-wave plate.

alkaline atom to an Ω_p “probe” pulse resonant to the “D2” transition can be altered by driving an “auxiliary” “D1” transition with an Ω_c control pulse. Here, a long enough control duration $\tau_c \gg 1/\omega_{\text{fs}}$ is required to resolve the fine-structure-split optical lines and to isolate the optical transitions under study. The control pulse also needs to be short, $\tau_c \ll 1/\Gamma_e, 1/\Gamma_a$ to avoid spontaneous emission from the excited $|e\rangle, |a\rangle$ states, and that $\tau_c \ll 1/\omega_{\text{hfs},g}, 1/\omega_{\text{hfs},a}$ is preferred so that the multi-level dynamics associated with hyperfine Raman excitations [35, 36] are relatively easy to manage (Appendix A). The laser of choice is a picosecond laser [33, 37, 38]. The ~ 100 GHz bandwidth is narrow enough to resolve atomic lines with multi-THz separations, wide enough to cover the typical hyperfine interaction at the GHz level, and support quick enough pulsed control to avoid radiation damping. Furthermore, a moderate Ω_c at the 100 GHz level is sufficient for the picosecond control. The moder-

ate strength helps avoiding *e.g.*, photon-ionization during multiple controls [39], and practically enable efficient implementation with low-energy pulses.

The light confinement enables efficient optical control at nanophotonic interfaces [40–45]. We consider the specific example of the ONF interface illustrated in Fig. 1, where the D1 transition of proximate ^{85}Rb atoms is controlled by transform-limited picosecond pulses of $\lambda_c = 795$ nm light guided through a step-index silica nanofiber [34] in the fundamental HE_{11} mode (Appendix B) [2]. At a $d = 500$ nm fiber diameter, about 20% of the light power propagates evanescently in vacuum to interact with atoms. The control is remarkably efficient. A resonant pulse energy of merely $\mathcal{E}_1(\pi) \sim 1$ pJ \cdot ps/ τ is sufficient to drive a $|g\rangle - |a\rangle$ population inversion near the ONF surface.

We are interested in the actual quality of the D1 inversion. Unfortunately, the strong optical confinement

(Fig. 1b) is associated with light intensity and polarization inhomogeneities [2, 46, 47] to prevent a simple pulse from achieving a uniform inversion in the near field, particularly in presence of the $|g\rangle - |d\rangle$ Raman couplings [35]. Nevertheless, it is important to note that when the control pulse is short enough, $\tau_c \ll 1/\omega_{\text{hfs},g}, 1/\omega_{\text{hfs},a}$, the hyperfine $|g\rangle - |a\rangle$ transition in the D1 example reduces to a $J_g = 1/2 \leftrightarrow J_a = 1/2$ transition, with the ratio of coupling strengths for the decoupled σ^\pm transitions to be determined by local ellipticity of light $\varepsilon(x, y) = |\mathbf{E}^* \times \mathbf{E}|/|\mathbf{E}|^2$ (The quantization axis is chosen along the local helicity axis $\mathbf{e}_h = \mathbf{E}^* \times \mathbf{E}/|\mathbf{E}|^2$). For the limiting case of a linearly polarized field, the coupling strengths become degenerate (Appendix A). One thus expect nearly perfect inversion at a specific intensity. This is confirmed with our full-level simulations (Appendix C) [36, 48, 49], illustrated in Fig. 1(c,i) with an example 2D distribution of $|g\rangle - |a\rangle$ inversion efficiency $f(x, y)$ for stationary, initially unpolarized atoms in $|g\rangle$. Here, for an linearly polarized control pulse in the HE_{11}^y mode with an incident ellipticity $\varepsilon_{\text{in}} = 0$ (Fig. 1a), the near-field ellipticity is minimized near $y = 0$ (Fig. 1b), $\varepsilon(x, y) \ll 1$ to support the nearly perfect inversion within $\tau_c = 6$ ps time. However, the inversion is not robust. A nanoscale shift of atomic position can degrade the performance substantially. Furthermore, the $f = 99\%$ contour (which is barely visible in Fig. 1(c,i)) vanishes at a moderate $\varepsilon_{\text{in}} = 0.1$ as illustrated in Fig. 1(c,ii). We note such a slight change of the HE_{11} polarization state [2] could easily be induced by the birefringence of the optical fiber.

To improve the control robustness, composite pulse sequence with N sub-pulses can be programmed to achieve highly accurate control with uniform efficiency by exploiting the geometric phase of 2-level transitions [50]. Such composite techniques are well developed in the research field of nuclear magnetic resonance (NMR) [25, 31, 32]. In particular, to invert the population of a 2-level spin, a sequence of N -pulses with equal amplitude $\{A_j\} = A$ and optimal phase $\{\varphi_j\}$, $j = 1, \dots, N$ is shown to be highly resilient to the field strength and the frequency detuning errors [31].

In the optical domain, the NMR-inspired composite technique can be exploited for driving ensemble of atoms illuminated by an inhomogeneous laser field, as well as for driving ensemble of transitions with different transition strengths (and slight different transition frequencies) for a same atom. The ONF-based atomic state control in this work exploits both aspects of the control technique (Appendix A). The composite pulses are synthesized within picoseconds [33, 51–53] for the aforementioned reasons associated with quantum control timescales. An incident single picosecond pulse, with energy \mathcal{E}_0 and a full pulse width at half maximum τ_0 , can be shaped into $j = 1, \dots, N$ sub-pulses with equal-spaced delays $\tau_j = (j-1)\tau_d$ and precisely programmable amplitudes $\{A_j\}$ and phases $\{\varphi_j\}$ (Fig. 2, see Sec. III A) [33]. Taking into account the sech^2 -shaped soliton pulses from a mode-locked laser [54], we associate a total control du-

ration $\tau_c = (N-1)\tau_d + \tau$ to the composite pulse with $\tau = 2\tau_0$ to characterize the control in the time domain.

A particular example of robust atomic state control at the ONF interface is illustrated in Fig. 1(c,iii) according to numerical simulation of ^{85}Rb atomic state dynamics driven by the near field composite D1 coupling. For the atom starting from an arbitrary Zeeman sub-level of $|g\rangle$ at $t = 0$, by optimizing the relative phases $\{\varphi_j\}$ among the sub-pulses of an $N = 5$ composite sequence, according to ref. [31], an $f > 99\%$ population inversion can be achieved around $y = 0$ across a substantial area in the near field (the purple contour in Fig. 1(c,iii)). The diameter along the narrower x -direction is $w \approx 110$ nm, substantially larger than the 1-pulse case (where even for the 95% contour the width is only $w \approx 40$ nm). Furthermore, as illustrated in Fig. 1(c,iv), the achieved population inversion is robust against small incident polarization variations. We thus expect robust implementation of the $N = 5$ composite sequence to *e.g.* arrays of trapped atoms through the ONF interface [3, 34, 55] to achieve ultra-precise atomic state control. The total control time is $\tau_c = 66$ ps in the Fig. 1 simulation, with a $\tau_0 = 3$ ps pulse width. More detailed elaborations of the near-field composite control, including the numerical methods, are given in Appendices A, B and C 1.

Beyond population inversion, composite pulses can be shaped to implement sophisticated control sequences [31, 32]. Importantly, for composite pulses with nearly equal amplitudes and arbitrary phases, the sub-pulse energy $\mathcal{E}_j < \mathcal{E}_0/N^2$ is limited by conservation of optical spectrum density. With the $\mathcal{E}_0 = N^2\mathcal{E}_1(\pi)$ scaling for the example of interest here and at a moderate pulse shaping efficiency [33], the required input pulse energy \mathcal{E}_0 for up to $N = 10^2$ sub-pulses is below 100 nJ for convenient implementations with a mode-locked laser. The \mathcal{E}_0 requirement is reduced further for nano-structures with better atom-light cooperativity [45, 56, 57].

We come back to the $N = 5$ scheme [31] in Fig. 1 and consider a 1D lattice gas trapped near ONF [3, 34, 55]. Following the $|g\rangle - |a\rangle$ inversion, another $N = 5$ composite pulse sending from the opposite direction can drive a return of the atomic ground state population. With β_c to be the ONF propagation constant (Fig. 1), a sub-wavelength-scale $e^{2i\beta_c z}$ geometric phase is patterned to atomic state $|g\rangle$. As such, freely excited $|g\rangle - |e\rangle$ dipole spin waves can be reversibly shifted into the subradiant domain on demand [10–12] to access interacting quantum optics in the confined geometry [1, 14, 15, 17–19, 21, 22].

III. A PROOF-OF-PRINCIPLE DEMONSTRATION

The experimental setup illustrated schematically in Fig. 1a follows a control-probe strategy. A D2 probe pulse resonant to the $|g\rangle - |e\rangle$ transition is combined with the picosecond D1 control pulses through a polarization-dependent beamsplitter and sent through the same ONF.

The D2 ONF transmission T is monitored. We expect the pulsed $|g\rangle - |a\rangle$ (D1) control to transiently deplete the ground state population ρ_{gg} in the near field and therefore reduces the evanescent-coupling induced attenuation of the guided D2 probe. The control-induced transient transmission δT is normalized by the unperturbed atomic absorption ΔT as $\overline{\delta T} \equiv \delta T / \Delta T$. In the linear regime of the D2 absorption where $\Delta T \propto \rho_{gg}$, a $\overline{\delta T} \approx \overline{f_g}$ relation is established to infer transient ground state population depletion $f_g(\mathbf{r}) \equiv \Delta\rho_{gg}(\mathbf{r})/\rho_{gg}$ from the first principle. In particular, $\overline{f_g}$ is numerically evaluated by spatially and thermally averaging the ground state depletion $f_g(\mathbf{r})$ weighed by the vectorial near-field coupling strength of the guided $\lambda_p = 780$ nm probe (Appendix C 4), according to either full (Appendix C 1) or simplified (Appendix D 1) model of D1 control dynamics based on optical Bloch equations [36].

Experimentally, the rubidium partial pressure at the nanofiber location is maintained around 10^{-5} Torr by electronically heating a dispenser ~ 30 cm away in the vacuum. Depending on the actual vapor pressure, a $\Delta T \approx 0.1 \sim 0.2$ reduction of ONF transmission is obtained by locking the probe laser to the F=2-F'=3 D2 hyperfine transition of ^{85}Rb . A heater attached to the ONF vacuum mount helps to maintain a local temperature of 90°C to suppress condensation of Rb atoms to the ONF surface. The probe beam is pulsed with a suitable duration $\tau_p = 2$ ns to match the transiently broadened optical response of atoms, as to be detailed shortly, and is sent to ONF after a Δt delay relative to the composite control. As in Fig. 1a, we combine the picosecond control (with $N \leq 3$ in this work) and nanosecond probe with a polarization beamsplitter (PBS) before coupling to the fiber. The polarization state of the ONF HE_{11} mode is controlled by a pair of computer-motorized half and quarter waveplates (Appendix E 2). After the light-atom interaction and to separate the probe pulse from the pump background at the ONF output, we split the combined beams with another PBS (not shown in Fig. 1) to filter each path with a holographic grating at “p” polarization with $\sim 70\%$ diffraction efficiency. The grating-filtered probe signals are then overlapped to a 1 GHz avalanche photodiode (APD) module (Hamamatsu C5658) after an additional interference filter to ensure negligible control pulse background. The APD signal is integrated by a home-made analogue signal integrator which compares 10^7 interleaved measurements with and without the control pulses in three seconds (Appendix E 1). The high speed differential measurements lead to quality signals capable of resolving δT at 1% level within 3 seconds of measurements, even though the probe power is kept at $P_p \approx 10$ nW to avoid saturating the D2 absorption. The transient change of transmission $\overline{\delta T}(\Delta t, \{A_i, \varphi_i\})$ is recorded for various composite pulse sequence at certain Δt delay. In between measurements, the value of ΔT for the $\overline{\delta T}$ normalization is monitored instead with a slow photo-multiplier tube (Hamamatsu CR131), by comparing the on-resonant transmission T with the off-resonant

values during laser frequency scans.

A. Pulse sequence generation system

Our nanofiber interface technique relies on coherent generation of composite sequence of picosecond pulses with precisely tunable amplitude and phase, $\{A_j, \varphi_j\}$, to optimize the atomic state inversion according to atomic physics and quantum control theory. The composite picosecond pulse generator is based on a time-domain pulse shaping method developed recently [33], as schematically illustrated in Fig. 2 and briefly summarized as following.

We use a Ti-Sapphire mode-locked laser (Spectra-Physics Tsunami system) to generate transform-limited picosecond pulses with $\tau_0 = 12$ ps at a repetition rate of $f_{\text{rep}} = 80$ MHz, referred to as $\mathbf{E}_{\text{in}}(t)$ in the following. The output is directed to a multi-frequency $\{\omega_j\}$ -driven double-pass acousto-optical modulator (AOM). Instead of retro-reflecting the multi-diffracted beams, we use a high-density grating (2400 line/mm) to retro-diffract each path backward for the second AOM diffraction. The grating retro-diffraction introduces a path-dependent delay $\tau_j = 2L_j/c \propto \omega_j - \omega_1$ relative to τ_1 . Among the AOM double-diffracted beams, the direction-reversed beam is picked by a polarization beamsplitter, repetition rate f_{rep} pre-scaled [58] and pulse-picked (not shown in Fig. 2), before being coupled into a single-mode fiber that is connected to ONF. In this work, the tunable delay for $\tau_j = (j-1)\tau_d$ is set by $\tau_d = 24$ ps. Taking into account an overall loss coefficient κ , the shaped composite pulse output to the ONF interface, as a sum of individually delayed sub-pulse $\mathbf{E}_{j,\text{out}}(t)$, can be expressed as [33]

$$\begin{aligned} \mathbf{E}_{\text{out}}(t) &= \kappa \sum_j^N \mathbf{E}_{j,\text{out}}(t), \\ &= \sum_j^N A_j e^{i\varphi_j} \mathbf{E}_{\text{in}}(t - \tau_j). \end{aligned} \quad (1)$$

The amplitudes and phases of the composite pulses $\{A_j, \varphi_j\}$ are controlled by that of the f_{rep} -synchronized rf waveforms $\{A_j^c, \varphi_j^c\}$ as $A_j \propto \kappa(A_j^c)^2$ and $\varphi_j = 2\varphi_j^c + \text{constant}$ offsets. As described in ref. [33], the multiple beams share a common optical path to be highly phase-stable. As a result, the composite pulse shaped by the rf-programmed multi-frequency AOM is amplitude and phase stable over hours.

B. Single pulse control

We first benchmark the ONF interface with a series of $N = 1$, single-pulse control-probe experiments. By scanning the probe-to-control pulse delay Δt , we investigate the transient optical response of the atomic vapor-nanofiber system to illustrate the mesoscopic nature of the nanoscale atomic vapor. We then demonstrate the highly efficient light-atom coupling with a full saturation of the control effect at sub-pico-Joule pulse energies. We also highlight the polarization dependence of the transient atomic response (Appendix E 2).

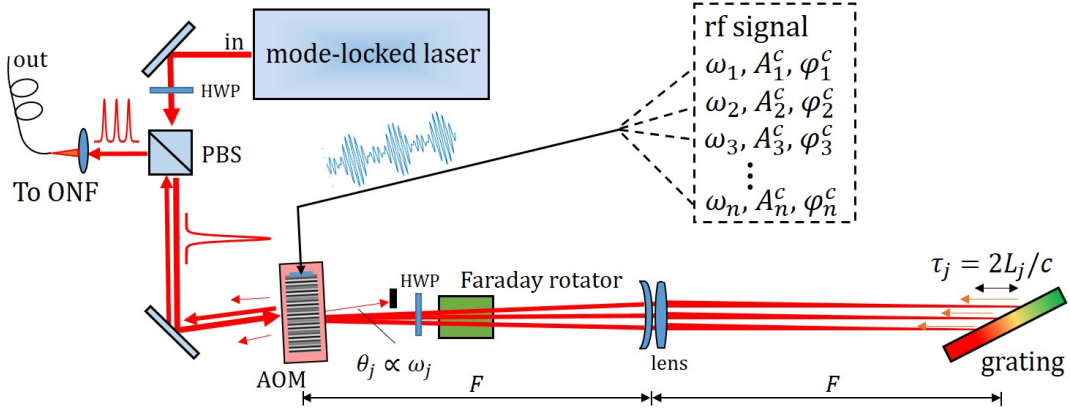


FIG. 2. Schematic of the picosecond pulse sequence generation system [33] for the ONF-interface atomic state control in this work. A transform-limited picosecond pulse is diffracted by a multi-frequency-driven acousto-optical modulator (AOM) into multiple paths, retro-diffracted by a grating to double-pass the AOM with tunable delay $\{\tau_j\}$. The output pulses along the time-reversed direction is separated from the input using a polarization beam splitter (PBS), repetition rate prescaled and pulsed picked (not shown), before being coupled to a single-mode fiber toward the nanofiber experiment. Here $\tau_j = (j-1)\tau_d$ with $\tau_d = 24$ ps. The amplitude and phase of each pulse, $\{A_j, \varphi_j\}$, is programmed by the amplitude and phase of radio-frequency (rf) sideband signals driving the AOM.

1. Transient optical response

As illustrated in Fig. 3a, the transient transmission $\overline{\delta T}$ is measured as a function of the control-probe delay Δt . We set the control pulse energy to be $\mathcal{E}_1 \approx 0.5$ pJ (Appendix E3) which is strong enough to substantially reduce the near-field attenuation of the D2 probe pulse by the evanescent D1 excitation. Typical results are plotted in Fig. 3b. Here we see a transient $\overline{\delta T}$ up to 45%, which decays rapidly with a time constant as short as 2 ns itself, suggesting ~ 500 MHz transiently broadened linewidth. For comparison, the Doppler broadened D2 linewidth is about 300 MHz for the free gas with the average thermal velocity $v_T \approx 300$ m/sec at 360 K.

The rapid recovery of probe transmission to the steady-state value, as in Fig. 3b, is due to the mesoscopic atomic transportation at the evanescent ONF interface (Fig. 3c). After the picosecond excitation, atoms at the vicinity of ONF transferred to either $|a\rangle$ or the other $F = 2$ hyperfine ground states $|d\rangle$ become invisible to the probe field, leading to the enhanced transmission. These atoms gradually leave the near field region and are replaced by incoming atoms in $|g\rangle$ both from far away and from ONF surface desorption. Since the sub-wavelength distance characterized by the $\xi \approx 200$ nm decay length is much smaller than the mean free path for the thermal atoms to transport the optical coherence, $l_c = v_T/\Gamma_e \approx 10$ μm , the optical response cannot be described by effective media theory based on local responses [59]. In Appendix D 1, the optical response is simulated by sampling the thermal atomic trajectories subjected to the impulse picosecond control according to Maxwell's velocity distribution. For the thermal atoms across the near field, the impact of D2 transmission by the transient surface-induced level shifts [59, 60] is expected to be moderate, and is ignored

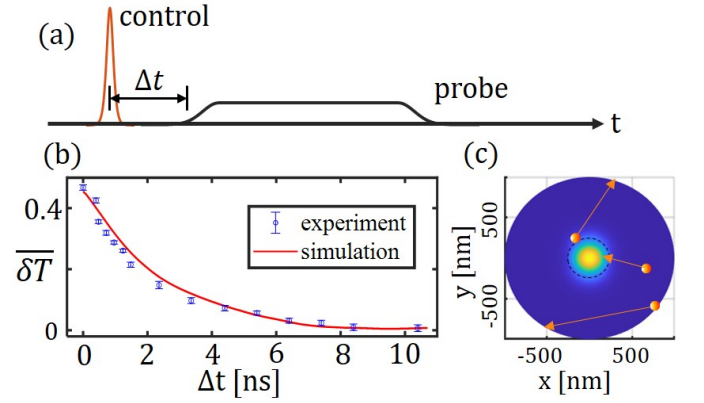


FIG. 3. Measurement on the transient optical response of the ONF-atomic vapor system. (a): Schematic timing sequence for the single-pulse control and probe measurement. (b): Experimental and simulation results of the transient change of probe transmission $\overline{\delta T}$ (Appendix E3) vs pump-probe delay Δt . The error-bars represent the statistical uncertainties from 10 repeated measurements. (c): Schematic illustration of thermal atoms trespassing the ONF evanescent field.

in the simplified analysis. By adjusting the effective pulse energy \mathcal{E}_1 for the 2-level simulation, the solid red curve in Fig. 3b agrees remarkably well with the measurements. As detailed in Appendix D 1, we expect more systematic measurement and analysis to unveil polarization-dependent dynamics [61] and even to resolve surface interaction at the nanometer/nanosecond scale [59, 60, 62].

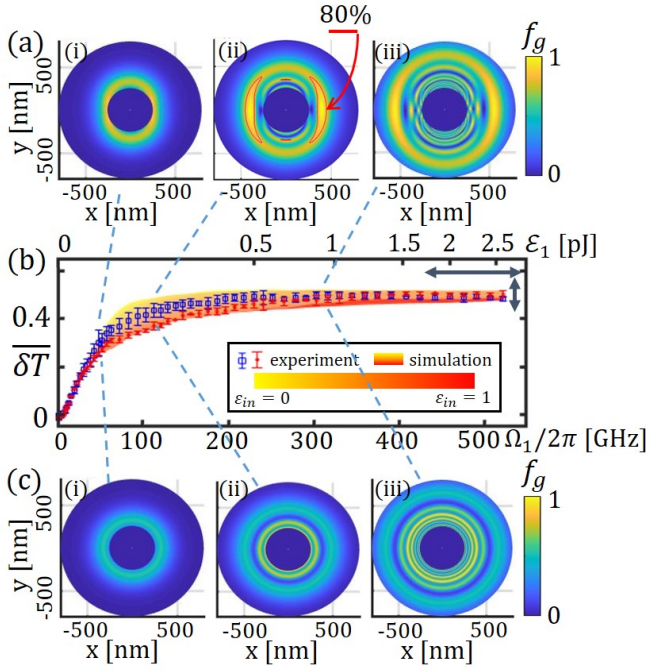


FIG. 4. Polarization-dependent saturation of picosecond excitation at a nanofiber interface. Figs. (a)(c) give the simulated transient population depletion $f_g(\mathbf{r})$ when a uniform vapor around ONF is subject to single pulse excitation with energy \mathcal{E}_1 . The incident HE₁₁ mode is linearly ($\epsilon_{in} = 0$) and circularly ($\epsilon_{in} = 1$) polarized for the Figs. (a)(c) simulations respectively. A $f_g = 80\%$ contour is highlighted in Fig. (a,ii). The numerically simulated $\overline{\delta T}$ at various incident ellipticities are given by Fig. (b) with the rainbow plot, color-coded by ϵ_{in} . The Ω_1 -axis is specified for the case of linearly polarized incidence. The experimentally measured $\overline{\delta T}$ as a function of \mathcal{E}_1 and associated peak Ω_1 are scatter-plotted with square ($\epsilon_{in} = 0$) and disk ($\epsilon_{in} = 1$) symbols, with error-bars estimated from three repeated measurements. To obtain the theoretical-experimental match in Fig. (b), the experimental \mathcal{E}_1 , Ω_1 , $\overline{\delta T}$ are uniformly rescaled (Appendix E3) within the measurement uncertainties, as suggested by the rescaling arrows on the top right.

2. Saturation of picosecond excitation

Enhanced atom-light interactions have been demonstrated previously at the nanofiber interface [42–45]. In presence of the highly inhomogeneous light intensity and ellipticity distributions (Fig. 1b), we expect the impulse control leading to spatially varying ground state population, with $f_g(\mathbf{r})$ oscillating between 0 and 1 in the near field. Therefore, immediately after the control pulse excitation with strong enough \mathcal{E}_1 , the evanescent coupling induced probe attenuation is expected to be transiently halved, as already suggested in Fig. 3b.

In this section, the simple picture of optical saturation is confirmed by detailed measurements of \mathcal{E}_1 -dependent $\overline{\delta T}$. To optimally retrieve the nonlinear signal, the $\tau_p = 2$ ns D2 probe is applied with $\Delta t = 0$ ps delay

(Fig. 3a). Typical transient transmission $\overline{\delta T}$ data are plotted in Fig. 4b as a function of pulse energy \mathcal{E}_1 and the peak Rabi frequency Ω_1 estimated at the ONF surface (Appendix E3). According to the numerical model to be discussed shortly, near $\mathcal{E}_1 \sim 0.2$ pJ, $\overline{\delta T}$ demonstrates substantial polarization dependence. In Appendix E2 we detail the HE₁₁ polarization control with automated polarization optics adjustments (Fig. 1). For the $\overline{\delta T}$ data here, the polarization states of control and probe beams are set to be linear ($\sim \text{HE}_{11}^{x/y}$ mode, blue square symbols) and circular (HE_{11}^{\pm} mode, red disk symbols) respectively. In both cases, nearly complete saturation of $\overline{\delta T}$ to approximately 45% occurs for the 2 ns probe, with \mathcal{E}_1 as small as 0.5 pJ.

We numerically simulate the D1 atomic state dynamics subjected to the vectorial light-atom interaction in the near field (Appendix C). With in mind the picosecond impulse is effectively instantaneous, the simulation is performed for static atoms uniformly distributed around the nanofiber to obtain $f_g(\mathbf{r})$. According to the experimental situation, we set unpolarized initial states with ground state occupancy $\rho_{gg}^{(0)} = 7/12$ and $\rho_{dd}^{(0)} = 5/12$ evenly populates the twelve ground-state Zeeman sublevels. Typical $f_g(\mathbf{r})$ plots are given in Fig. 4(a)(c) for the case of linear and circular HE₁₁ modes of control respectively. As in Fig. 4a and explained in Appendix C3, the ground state population can be nullified in the near field where the polarization is purely linear. For comparison, the reduced D1 depletion efficiency for the circular incident polarization in Fig. 4c is associated with local ellipticity $\epsilon \approx 0.95$ (Appendix B) so the σ^{\pm} coupling strengths are different substantially to prevent simultaneous efficient excitations. On the other hand, the nearly ϵ_{in} -independent $\overline{\delta T}$ saturation at large \mathcal{E}_1 as in Fig. 4b is a result of near-field chirality [46] which prevents completely circular excitation with $\epsilon(x, y) = 1$ from uniformly occurring in the near field.

To evaluate the polarization-dependent response of the mesoscopic vapor with a full-level Monte-Carlo simulation is computationally demanding. As detailed in Appendix D, we find that $\overline{\delta T} \approx \overline{f_g}$ can be approximately evaluate as a sum of stationary atomic response according to the evanescent probe coupling. To effectively account for atomic motion during the $\tau_p = 2$ ns probe, the evanescent coupling is smoothed over an average thermal diffusion length $\xi_p' \approx v_T \tau_p / 2$ first [61], before the evaluation of optical attenuation by the surrounding vapor. The estimated $\overline{\delta T}$ according to the simulation is presented in Fig. 4b with various ellipticity for the incident control and probe polarizations. The experimentally measured data are matched to the simulation, by linearly rescaling the $\overline{\delta T}$, \mathcal{E}_1 and Ω_1 axes within the uncertainties by the $\overline{\delta T}$ and laser power measurements (Appendix E3). Similar to the Fig. 3 results, here the remaining discrepancies in Fig. 4 is not completely understood, but may be resolved by more accurately modeling the tapered ONF interface [34].

C. Robust composite control

We now demonstrate robust population inversion at the ONF interface. This is achieved by implementing the composite technique prescribed by ref. [31] with our picosecond pulse sequence generator. Due to technical reasons to be discussed in Sec. IIID, we limit the sub-pulse number to $N = 3$ in this demonstration.

As outlined in Sec. III A, the picosecond sequence is generated by shaping the $\tau_0 = 12$ ps pulses into three sub-pulses with a $\tau_d = 24$ ps inter-pulse equal delay, equal amplitudes $\{A_j\}$, and independently programmable phases $\{\varphi_j\}$. At a fixed pulse energy, we perform 2D scan of the relative phases $\Delta\varphi_{1,3} = \varphi_1 - \varphi_3$ and $\Delta\varphi_{2,3} = \varphi_2 - \varphi_3$ in small steps to record the transient transmission $\overline{\delta T}$. Typical results are presented in Fig. 5. As in Figs. 5(a)(d), the moderate $\tau_d = 2\tau_0$ leads to partially overlapping sub-pulses. With accurate numerical modeling in Appendix C to account for the overlap, the composite scheme is effectively captured by non-overlapping pulses, as assumed in the following.

At low pulse energy, we expect the picosecond control to be most efficient when $\Delta\varphi_{1,3} = \Delta\varphi_{2,3} = 0$ so the resonant spectra density to $|g\rangle - |a\rangle$ excitation is maximized. This is the case in Fig. 5e according to the simulation where the equal-phase point with optimal $\overline{\delta T}$ is marked with “O”. The corresponding optical waveform is plotted in Fig. 5a on the top. The transient ground state depletion $f_g(\mathbf{r})$, similar to those in Fig. 4(a.i) for the single pulse with similar total pulse area, is displayed in the middle. Indeed, for the equal-phase case, the 3-pulse control is equivalent to a single-pulse control with an elongated duration τ_c . Therefore, the control dynamics is not robust against variation of optical intensity (nor polarization), as suggested by the simplified 2-level Bloch sphere dynamics in the bottom plot of Fig. 5a.

However, with increased single-pulse energy $\{\mathcal{E}_j\}$ and the associated peak Rabi frequency $\{\Omega_j\}$, a transition of the optimal $\{\varphi_j\}$ occurs around $A_j \approx \pi/3$ pulse area defined as $A_j = \int \Omega_j dt$ near the ONF surface. Beyond the point, the optimal φ_2 takes non-zero values relative to the equal $\varphi_{1,3}$. This is suggested by the simulations in Figs. 5(e-h), which agree globally with the Figs. 5(j-m) experimental measurements without freely adjustable parameters. In particular, with an optimal $\Omega_j \approx 2\pi \times 75$ GHz and when ONF incident polarization is linear (Fig. 5(h,m)), transient transmission $\overline{\delta T} \sim 70\%$ are found at two phase combinations with $\varphi_2 = \pm\pi/2$, $\varphi_{1,3} = 0$. For the case of $\varphi_2 = \pi/2$, our full level simulations suggest that the transient transmission $\overline{\delta T}$ integrated over $\tau_p = 2$ ns is supported by transient depletion of the $|g\rangle$ state population with $f_g(\mathbf{r}) > 80\%$ (Fig. 5b), over a connected area at the ONF proximity by the picosecond impulse control to be substantially larger than the 1-pulse case (Fig. 4a). This population depletion is largely due to the $|g\rangle - |a\rangle$ inversion with $f(\mathbf{r}) > 80\%$ albeit across a slightly smaller area.

The efficient population inversion across the highly in-

homogeneous near field, as suggested by the Fig. 5(h,m) data, is a result of 2-level geometric robustness inherent to the composite control [50] (Also see Appendix A). As illustrated in Fig. 5d, the “redundant” SU(2) rotation enables robust $|g\rangle - |a\rangle$ inversion for the 3-pulse control between $A_j = 0.5\pi \sim \pi$ when φ_2 takes the value of $\pm\pi/2$ relative to $\varphi_{1,3}$. In both cases, the rotation by the 2nd sub-pulse automatically cancels out the extra rotations by the first and the third sub-pulses. We also refer readers to Fig. 1c for the $N = 5$ example [31], where the full-level simulation suggests nearly perfect inversion near the ONF interface around $A_j = \pi$.

We finally remark on Raman transitions driven by the composite pulse with the fairly long $\tau_c \approx 1/\omega_{\text{hfs},g}$ duration. As in Fig. 5b, compared to the expected inversion efficiency $f(\mathbf{r})$, the ρ_{gg} -depletion efficiency $f_g(\mathbf{r})$ is larger, which is a result of directional $|g\rangle \rightarrow |d\rangle$ transfer at $\varphi_2 = \pi/2$. Similarly, not shown in Fig. 5b is the “A” point with $\varphi_2 = -\pi/2$, where an opposite $|d\rangle \rightarrow |g\rangle$ transfer leads to reduced $f_g(\mathbf{r})$ relative to $f(\mathbf{r})$. However, in neither case these Raman contributions notably affect the apparent $\pm\pi/2$ symmetry in the transmission $\overline{\delta T}$ in Figs. 5(e-h) and Figs. 5(j-m), since when the local polarization is approximately linear ($\varepsilon(\mathbf{r}) \ll 1$, Fig. 1b), the Raman transitions are largely suppressed as long as $\omega_{\text{hfs},a}\tau_c \ll 1$ [63]. On the other hand, in Fig. 5(i,n) $\overline{\delta T}$ at $\varphi_2 = -\pi/2$ (the “C” point) is substantially smaller than that for $\varphi_2 = \pi/2$ (the “D” point). The broken sign symmetry is associated with substantial $|g\rangle \leftrightarrow |d\rangle$ Raman transfer, as unveiled by comparing $f_g(\mathbf{r})$ with $f(\mathbf{r})$ in Fig. 5c according to the full-level simulations. Here, with the control light in the circularly polarized HE_{11}^σ mode, the ellipticity in the near field is substantially larger (Appendix B). With atoms randomly initialized in $|g\rangle$ and $|d\rangle$, the apparently inefficient depletion $f_g(\mathbf{r})$ at $\varphi_2 = \pi/2$ in Fig. 5c is associated with substantial $|d\rangle \rightarrow |g\rangle$ transfer which negatively offsets the enhanced transmission by $|g\rangle - |a\rangle$ inversion. Similarly, not shown in Fig. 5 are $f_g(\mathbf{r}) > f(\mathbf{r})$ at “D” point with $\varphi_2 = \pi/2$, as those in Fig. 5b but by a wider margin due to the more efficient $|g\rangle \rightarrow |d\rangle$ transfer.

D. Toward larger N

The $N = 3$ composite picosecond control relies on an ergodic search of optimal pulse parameters in the parameter space. As in Fig. 5, the method supports detailed investigation of the control dynamics across the parameter space by comparing the experimental measurements with theory. On the other hand, the “brutal force” approach becomes impractical at larger N , particularly when the search time is constrained by slow experimental cycles. Ideally, the relative amplitude and phase $\{A_j, \varphi_j\}$ should be directly programmed into an N -pulse sequence generator according to the optimal control theory of accurately modeled experimental system. When the physical model of either the interaction or the pulse shaper itself is not

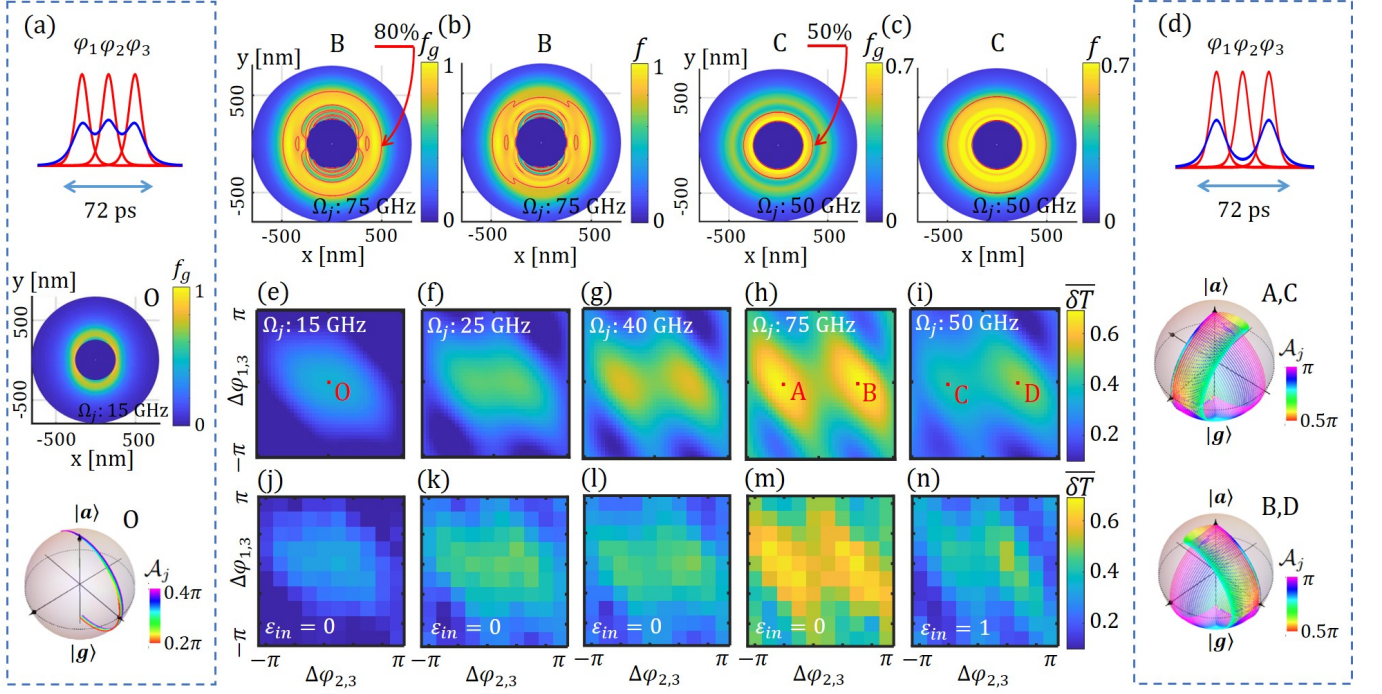


FIG. 5. Three-pulse atomic state control through the ONF interface. (a): The sub-pulse intensity (red line) and total in-phase amplitude (blue line) are plotted for an $N = 3$ sequence shaped from a transform-limited $\tau_0 = 12$ ps pulse with $\tau_d = 24$ ps inter-pulse delay and equal $\varphi_{1,2,3} = 0$. Simulated transient population depletion $f_g(\mathbf{r})$ for the experimental condition marked with “O” in Fig. (e) is given in the middle. The associated Bloch sphere 2-level dynamics is given in the bottom. More generally, simulated transient transmission $\overline{\delta T}$ vs $\Delta\varphi_{1,3}$, $\Delta\varphi_{2,3}$ are plotted in Figs. (e-i), assuming control pulses in the HE_{11}^y mode $\varepsilon_{\text{in}} = 0$, except for Fig. (i) where the circular HE_{11}^z mode is assumed ($\varepsilon_{\text{in}} = 1$). Here the $\overline{\delta T}$ values are numerically averaged from $f_g(\mathbf{r})$, as described in the text. The $f_g(\mathbf{r})$ for the $\{\varphi_j\}$ combination marked with “B” in Fig. (h) and “C” in Fig. (i) are respectively given in Fig. (b) and Fig. (c), where $|g\rangle - |a\rangle$ population inversion efficiencies f are plot for comparison. The $f_g = 80\%$ and $f = 80\%$ contours are marked in Fig. (b) to be compared with those in Fig. 4a. Also, the $f_g = 50\%$ and $f = 50\%$ contours are marked in Fig. (c). Similar to Fig. (a), the pulse profiles with $\varphi_j = \{0, \pm\pi/2, 0\}$ are given in Fig. (d), together with the representative Bloch sphere dynamics sketched below. Figs. (j-n) are experimental $\overline{\delta T}$ data to be compared with Figs. (e-i). Similar to Fig. 4b, the experimental Ω_j , $\overline{\delta T}$ values are globally re-scaled to match the simulations, within the uncertainty of the measurements (Appendix E 3).

accurate, then a close-loop approach should be followed for in situ optimizing of pulse parameters, similar to the pioneer works in nonlinear optics [64, 65].

Efforts toward composite control at larger N in this work is frustrated by a pulse shaper parameter cross-talk, as mentioned in ref. [33]. As being discussed there, the cross-talk is associated with acousto-optical transduction, in particular the nonlinearity of multi-frequency rf amplification for driving the single AOM in this work (Sec. III A). The cross-talk leads to enough complexity to prevent us from precisely modeling the shaper itself when operating at the required efficiency for $N \geq 5$. The cross-talk was also large enough to prevent a successful “close-loop” optimization. Toward directly programming optimal picosecond control, we are currently working on improving the pulse shaper for efficient arbitrary sequence generation at large N [66].

IV. SUMMARY AND OUTLOOK

A fundamental quest in nanophotonics is to enhance optical nonlinearities through confinements. The enhancements are not only instrumental to realizing efficient nonlinear optics and spectroscopy [40, 41], but also may support controllable interaction mediated by single confined photons, for exploring novel quantum state of matter in the optical domain [1]. In this work, we suggest that an enabling technique in the nonlinear quantum optical scenario is to optically control atomic states through the nanophotonic interface with qubit-level precision. We numerically demonstrate that the precise atomic state control with $f > 99\%$ fidelity can be achieved in the near field with composite techniques [25, 31, 32], by exploiting geometric robustness of electric dipole transitions at the picosecond time scale.

Experimentally, this work takes a first step toward precise nanophotonic control with the composite picosecond

scheme. An optimally phased $N = 3$ sequence is demonstrated to robustly invert the population of free-flying atoms across an optical nanofiber. In particular, the $\sim 70\%$ reduction of the evanescently coupled probe absorption, integrated over nanoseconds, strongly suggests $f > 80\%$ population inversion uniformly achieved around the nanofiber in the near field. The accurate implementation of the composite scheme is further confirmed by matching the measurements with elaborated modeling of the mesoscopic light-atom interaction.

We expect further development of the picosecond composite scheme for sophisticated nanophotonic atomic state controls. Besides enabling the nonlinear quantum optical scenarios as mentioned earlier, the flexible composite technique may open interesting perspectives in fundamental research such as to enable arbitrary electric dipole control in the near field by driving universal qubit gates [32], to achieve error-resilient atomic spectroscopy [67, 68], and to probe atom-surface interaction [69, 70] through an investigation of the optical properties of mesoscopic vapour [59] with an unprecedented level of control flexibility.

ACKNOWLEDGEMENT

We thank Professor Darrick Chang for very helpful discussions. We acknowledge support from National Key Research Program of China under Grant No. 2016YFA0302000 and No. 2017YFA0304204, from National Natural Science Foundation of China under Grant No. 12074083, 61875110, 62105191, 62035013, 62075192.

DATA AVAILABILITY

Data and simulation codes underlying the results presented in this paper are not publicly available at this time but may be obtained from the authors upon reasonable request.

Appendix A: Composite control of an $I = 0$ atom

In this section, we consider application of the composite technique to invert the state population of a fictitious atom without hyperfine structure ($I = 0$), by driving the $J_g = 1/2 \rightarrow J_a = 1/2$ D1 line with free-space optical pulses.

As in Fig. 6, the quantization axis for the light-atom interaction is naturally chosen along the \mathbf{k} direction. More generally, for the incident control field whose polarization state is characterized by the helicity vector,

$$\mathbf{e}_h = \mathbf{E}_c^* \times \mathbf{E}_c / |\mathbf{E}_c|^2, \quad (\text{A1})$$

the D1 transition is decomposed into σ^+ and σ^- transitions along the \mathbf{e}_h quantization axis, with the respective

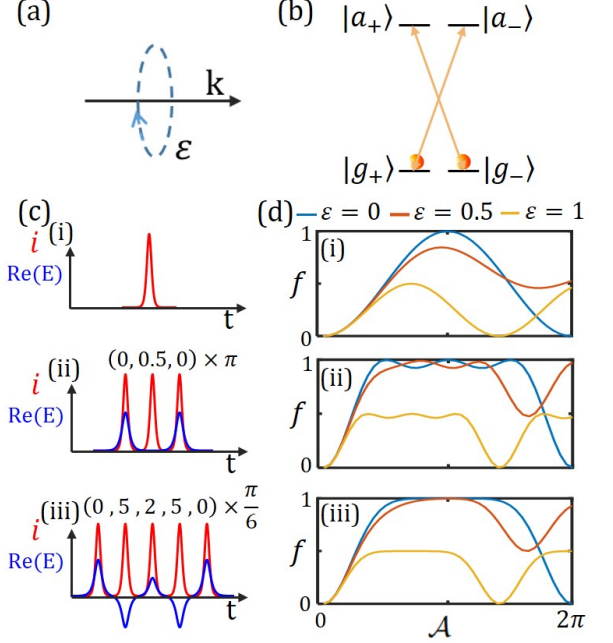


FIG. 6. Composite D1 inversion in absence of hyperfine interaction (nuclear spin $I = 0$). The level diagram for the degenerate $S_{1/2} - P_{1/2}$ transition is given in (b). The quantization axis is set along the light helicity vector $\mathbf{e}_h = \mathbf{E}_c^* \times \mathbf{E}_c / |\mathbf{E}_c|^2$, which is parallel to the \mathbf{k} -direction for the free field example in Fig. (a). The ellipticity is defined as $\varepsilon = |\mathbf{e}_h|$. Fig. (d) gives numerical results on population inversion efficiency f at different ε for 1, 3, and 5 picosecond pulses, as a function of single pulse area defined as $\mathcal{A} = \int \Omega_c dt$ according to Eq. (A4). The Fig. (c) plots on the left illustrate the corresponding time-dependent intensity (i , red line) and in-phase quadrature ($\text{Re}[\mathbf{E}]$, blue line) of the pulses, with relative phases according to ref. [31] marked on the top.

Rabi coupling strengths

$$\begin{aligned} \tilde{\Omega}_c^+(\mathbf{r}, t) &= \sqrt{2} \cos(\theta/2) \Omega_c(\mathbf{r}, t) \\ \tilde{\Omega}_c^-(\mathbf{r}, t) &= \sqrt{2} \sin(\theta/2) \Omega_c(\mathbf{r}, t). \end{aligned} \quad (\text{A2})$$

Here $\theta \in [0, \pi/2]$ is associated with the field ellipticity

$$\varepsilon = |\mathbf{e}_h| \quad (\text{A3})$$

as $\varepsilon = \cos\theta$. The Rabi frequency Ω_c is defined as

$$\Omega_c(\mathbf{r}, t) = \frac{|\mathbf{E}_c(\mathbf{r}, t)|}{\hbar} \frac{1}{\sqrt{3}} |\langle J_g || \mathbf{d} || J_a \rangle|. \quad (\text{A4})$$

It is important to note that to use Eqs. (A1)(A2) for the linearly polarized light, the quantization axis needs to be chosen perpendicular to the polarization vector itself, i.e., as a limiting case of small ε .

In the following within this section we consider $\Omega_c(\mathbf{r}, t) = \Omega_c(t)$ and $\mathbf{e}_h(\mathbf{r}) = \mathbf{e}_h$ to be spatially uniform. Our goal is to design certain pulse sequences to invert the

population of the reduced D1 system initialized in the unpolarized ground state, $\rho(0) = \frac{1}{2}(|g_+\rangle\langle g_+| + |g_-\rangle\langle g_-|)$. This is investigated with the simulation method outlined in Appendix C1 by solving the Schrodinger equation for a control time τ_c and then evaluate $f = \rho_{aa} \equiv \rho_{a_+a_+} + \rho_{a_-a_-}$, for the $J_g = 1/2 \leftrightarrow J_a = 1/2$ transition.

Clearly, the Rabi frequencies for the σ^\pm couplings by Eq. (A2) are equal only for linearly polarized light. For general polarization state, it is not possible to simultaneously invert the two sub-spins with $N = 1$ single “ π ”-pulse (Fig. 6(c,i)). In fact, in the limiting case of circular polarized π -pulse (Fig. 6(d,i), the yellow curve with $\varepsilon = 1$), only 50% of ground-state population can be inverted, albeit with a $\sqrt{2}$ -times larger Rabi oscillation frequency relative to the linear polarized case (Fig. 6(d,i), the blue curve with $\varepsilon = 0$). For the linear case, the perfect inversion at $\mathcal{A} = \pi$ scales as $\rho_{aa}(\tau_c) = \sin^2(\mathcal{A}/2)$ and is therefore quite sensitive to the pulse area $\mathcal{A} = \int \Omega_c dt$, requiring perfect control of light intensity.

For comparison, in Fig. 6(d,ii) and Fig. 6(d,iii) the population inversion efficiencies are shown for a composite 3-pulse (Fig. 6(c,ii)) and 5-pulse (Fig. 6(c,iii)) sequence respectively. Both sequences follow prescription by ref. [31] as $\mathcal{A}_j = \mathcal{A}$ close to π and phase $\{\varphi_j\} = \{0, \pi/2, 0\}$, $\{0, 5\pi/6, \pi/3, 5\pi/6, 0\}$ for the 3- and 5-pulses. The 3-pulse sequence is experimentally exploited in Sec. III C. Comparing with the single pulse inversion in Fig. 6(d,i) that is perfected only for linearly polarized light at $\mathcal{A} = \pi$, the composite pulse schemes is much more tolerant to deviation of \mathcal{A} from π , and can achieve $f \rightarrow 1$ even by elliptically polarized excitations.

For isolated 2-level systems, the error-resilient performance of composite pulses improves with pulse number N [31, 32], but to apply the technique to an optical transition of “real” atoms, perturbations from vacuum fluctuation and the multi-level dynamics put additional constraints to the optimal pulse bandwidth $\Delta f \sim 1/\pi\tau_0$ and the total duration τ_c , as being emphasized in Sec. II of the main text. In this section, we have shown that if the hyperfine splitting can be ignored, then the composite pulse can operate well within a fine-structure manifold – the D1 line. The composite control on the D2 line is similar and will not be discussed in this work. As to be shown in Appendix. C1, practically it is not always possible to completely ignore the hyperfine interaction, in which case we still numerically verify that the 2-level geometric robustness [50] of the D-line transitions can be exploited to perfect the atomic state control by picosecond pulses with approximately linear polarization.

Appendix B: The HE_{11} mode

Aided by precise knowledge of the nanofiber geometry [34], we follow ref. [2] to calculate the optical field distribution around the nanofiber for the guided HE_{11} mode at specific wavelength. The intensity and ellipticity distribution for the control laser at $\lambda_c = 795$ nm, for

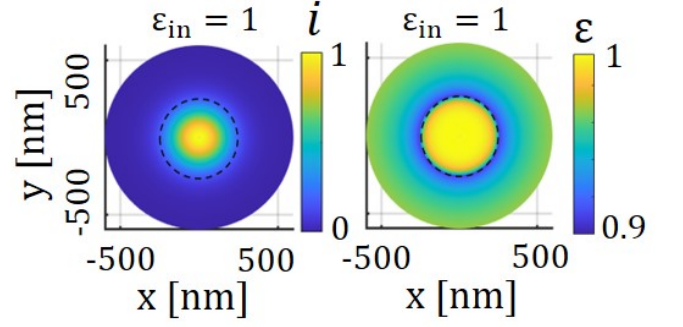


FIG. 7. Near field distribution of the normalized light intensity $i(x, y)$ and ellipticity $\varepsilon(x, y)$ for the circular HE_{11}^+ mode of the ONF in this work at $\lambda_c = 795$ nm.

the case of linearly polarized HE_{11}^y mode with incident ellipticity $\varepsilon_{\text{in}} = 0$ is presented in Fig. 1b, where one see the near field $\mathbf{E}_{\text{HE}_{11}^y}$ is linearly polarized around $y = 0$ with $\varepsilon(\mathbf{r}) \ll 1$. On the other hand, for control pulses with circular polarized HE_{11}^+ mode with incident ellipticity $\varepsilon_{\text{in}} = 1$, the electric field $\mathbf{E}_{\text{HE}_{11}^+} = \mathbf{E}_{\text{HE}_{11}^x} + i\mathbf{E}_{\text{HE}_{11}^y}$ has a local ellipticity $\varepsilon(\mathbf{r}) \approx 0.95$ which is substantially larger as shown here in Fig. 7. Similar mode intensity and polarization distributions are numerically evaluated for the probe pulse at $\lambda_p = 780$ nm.

More generally, for ONF excited with an incident $\varepsilon_{\text{in}} = \cos(\Theta)$ ellipticity, with an angle ϕ between the incident elliptical axis and the x -axis, the guided mode is a coherent superposition of the HE_{11}^+ and HE_{11}^- modes weighted by $\cos(\Theta/2)$ and $\sin(\Theta/2)$. The complex field is given by

$$\mathbf{E}(\mathbf{r}) = \cos\left(\frac{\Theta}{2}\right)e^{i\frac{\phi}{2}}\mathbf{E}_{\text{HE}_{11}^+} + \sin\left(\frac{\Theta}{2}\right)e^{-i\frac{\phi}{2}}\mathbf{E}_{\text{HE}_{11}^-}. \quad (\text{B1})$$

The normalized intensity distribution $i(\mathbf{r})$ and ellipticity distribution $\varepsilon(\mathbf{r})$ can be evaluated accordingly. The spatial profile of the evanescent field is equipped to evaluate the light-atom interaction to be detailed in the following.

Appendix C: Light-atom interaction – stationary atoms

The level diagram for the full D1/D2 electric dipole interaction is summarized in Fig. 8a. For the convenience of numerical calculation, we choose the ONF guiding direction \mathbf{e}_z , along which the field intensity and polarization distributions are invariant, as the fixed atomic quantization axis. The choice of local helicity axis as quantization axis will be discussed in Appendix C3. To conveniently formulate the multi-level vectorial interactions, we introduce Dirac kets $|g_m\rangle, |d_m\rangle$ to label the Zeeman sublevels of the hyperfine ground states. Similarly, the excited state Zeeman sublevels are label by $|a_m\rangle, |e_m\rangle$. The a, e symbols also index the total angular momentum F of the corresponding hyperfine levels [36].

Numerical analysis can in principle be performed using the full light-atom interaction Hamiltonian on the D1/D2 line. However, here our main focus is the D1 control dynamics [10]. The nano-Watt level D2 probe is weak enough in the linear response regime to support a simpler treatment for thermal atoms in this work. We therefore first model the picosecond D1 control dynamics, and then perturbatively derive its influence on the optical response of the ONF-atom system to the D2 probe.

1. Full model of the picosecond D1 interaction

We consider spectrum transform-limited picosecond D1 pulses from a mode-locked laser with a temporal amplitude profile $\mathcal{P}(t) = \text{sech}(1.76t/\tau_0)$ [54]. After time-domain pulse shaping [33], the composite sequence is sent through ONF to interact with atom at location \mathbf{r} . The pulsed optical field at the ONF interface is described by a slowly-varying envelop function

$$\mathbf{E}_c(\mathbf{r}, t) = \mathbf{E}(\mathbf{r})S_N(t), \quad (\text{C1})$$

with a spatial profile according to Eq. (B1), and temporally following the composite profile

$$S_N(t) = \sum_{j=1}^N A_j e^{i\varphi_j} \mathcal{P}(t - (j-1)\tau_d), \quad (\text{C2})$$

with $|A_j| \leq 1$ and $\tau_d \gg \tau_0$.

With the atomic states defined earlier, the Rabi frequencies to drive the $|g\rangle - |a\rangle$ and $|d\rangle - |a\rangle$ transitions are written as

$$\Omega_{a_n c_m}^l(\mathbf{r}, t) = \langle a_n | \mathbf{E}_c(\mathbf{r}, t) \cdot \mathbf{d}_l | c_m \rangle / \hbar \quad (\text{C3})$$

for all the $c = g, d$ states. Here \mathbf{d}_l with $l = -1, 0, 1$ are the electric dipole operators of the atom along $\{\mathbf{e}_-, \mathbf{e}_z, \mathbf{e}_+\}$ directions respectively. Therefore, $n = m + l$ is required by conservation of the magnetic quantum number. More generally, with the Clebsh-Gordan coefficients $\mathcal{C}_{a_n c_m}^l$ and the D1 Rabi frequency defined in Eq. (A4), the Rabi frequencies can also be written as $\Omega_{a_n c_m}^l(\mathbf{r}, t) = \sqrt{3}\Omega_c(\mathbf{r}, t)\mathcal{C}_{a_n c_m}^l$.

The D1 electric-dipolar interaction under the rotating wave approximation is written as

$$H_{D1}(\mathbf{r}, t) = \hbar \sum_a (\omega_a - \omega_{a0}) \sigma^{a_n a_n} + \hbar \sum_{c=g,d} (\omega_c - \omega_{g0}) \sigma^{c_m c_m} + \frac{\hbar}{2} \sum_{c=g,d} \sum_j \Omega_{a_n c_m}^j(\mathbf{r}, t) \sigma^{a_n c_m} + \text{h.c.} \quad (\text{C4})$$

Here an implicit summation of repeated n, m indices are assumed. The ω_{a0}, ω_{g0} are decided by the energy of reference level in the $5P_{1/2}$ and $5S_{1/2}$ electronic states respectively, chosen as the top hyperfine levels in this work. The control Rabi frequencies are accordingly written in the $\omega_{e0, g0}$ frame. The Pauli matrices are defined as $\sigma^{a_n c_m} = |a_n\rangle\langle c_m|$, similarly for $\sigma^{a_n a_n}$ and $\sigma^{c_m c_m}$.

With the Eq. (C4) Hamiltonian, we integrate the evolution operator $U(\mathbf{r}) = T e^{-i \int_0^t H_{D1}(\mathbf{r}, t') dt' / \hbar}$ to propagate electronic state of stationary atom at location \mathbf{r} . Related to possible geometric phase control of $|g\rangle - |e\rangle$ hyperfine optical coherence on the D2 line, we are particularly interested in high quality $|g\rangle - |a\rangle$ inversions [10]. The operation fidelity is characterized by an average inversion efficiency $f = \langle f_m \rangle_m$, with

$$f_m(\mathbf{r}) = \langle g_m | U^\dagger(\mathbf{r}) \mathbf{1}_a U(\mathbf{r}) | g_m \rangle. \quad (\text{C5})$$

Here $\mathbf{1}_a = \sum_{a,n} |a_n\rangle\langle a_n|$ is the projection operator into the $5P_{1/2}$ “ $|a\rangle$ ” manifold. We similarly define $\mathbf{1}_g = \sum_m |g_m\rangle\langle g_m|$ and $\mathbf{1}_d = \sum_m |d_m\rangle\langle d_m|$.

In addition, related to the experimental observation in this work is a normalized ground state depletion efficiency for an initially unpolarized atom, defined as $f_g(\mathbf{r}) = (\rho_{gg}^{(0)} - \rho_{gg}(\mathbf{r})) / \rho_{gg}^{(0)}$ with

$$\rho_{gg}(\mathbf{r}) = \text{tr}(U(\mathbf{r}) \rho^{(0)} U^\dagger(\mathbf{r}) \mathbf{1}_g). \quad (\text{C6})$$

The initial unpolarized atomic state is described by the density matrix $\rho^{(0)} = \frac{1}{12}(\mathbf{1}_g + \mathbf{1}_d)$ for ^{85}Rb to mimic the experimental situation. Accordingly we have $\rho_{gg}^{(0)} = 7/12$.

Finally, to facilitate the evaluation of D2 linear absorption later, the population and coherence of the hyperfine $|g\rangle$ level after the picosecond control are calculated according to

$$\rho_{g_m g_{m'}}(\mathbf{r}) = \langle g_m | U(\mathbf{r}) \rho^{(0)} U^\dagger(\mathbf{r}) | g_{m'} \rangle. \quad (\text{C7})$$

2. Numerical implementation

Numerical evaluation of $f(x, y)$, $f_g(x, y)$ according to Eqs. (B1-C5), as those in Fig. 1, Fig. 4, Fig. 5 in the main text, are implemented in a straightforward manner with Matlab [36]. It is important to note that for the picosecond control under investigation, the radiation damping at tens of nanoseconds scale decided by $\Gamma_a \approx 1/27 \text{ ns}^{-1}$ is ignored. For longer pulses and particularly when the radiation damping is enhanced collective in a lattice trap [34, 71], a stochastic wavefunction approach should be followed [48, 49, 72] in future work.

3. The $|J, I, m_J, m_I\rangle$ basis

Although the picosecond D1 interaction can be evaluated numerically, the underlying physics can be obscured by the apparently complicated multi-level, multi-photon couplings. In Appendix A we have already illustrated a simpler situation of D1 transition dynamics without hyperfine structure. The picture is also valid for atoms with hyperfine splitting, if the optical excitation is short enough: $\tau_c \ll 1/\omega_{\text{hfs},g}, 1/\omega_{\text{hfs},a}$.

Similar to the $I = 0$ case illustrated in Fig. 6b, by ignoring the hyperfine splitting, the light-atom interaction

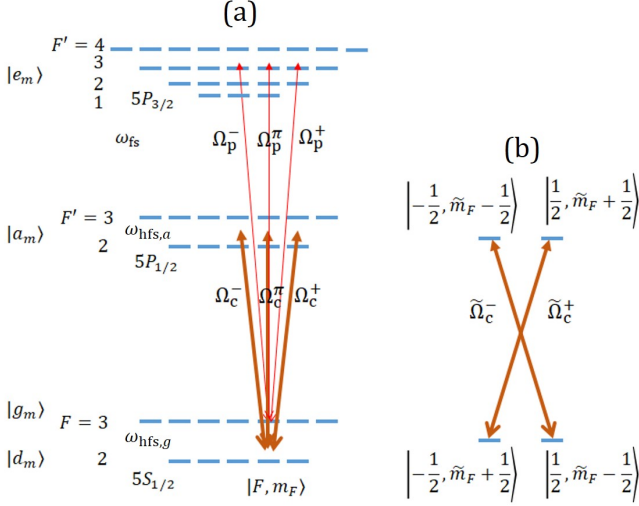


FIG. 8. (a): The full level representation of the Fig. 1d scheme in the main text. With a fixed quantization axis along z , the local $\mathbf{E}_{p,c}(\mathbf{r})$ could be decomposed into $\mathbf{e}_{\pm,z}$ directions to drive the $\Omega_{p,c}^{\pm,\pi}$ couplings respectively. (b): For the picosecond \mathbf{E}_c with $\tau_c \ll 1/\omega_{\text{hfs},g}, 1/\omega_{\text{hfs},a}$, a more convenient choice is to decompose along the local helicity axis \mathbf{e}_h (Eq. (A1)), leading to decoupled $\tilde{\Omega}_c^{\pm}$ couplings in the $|m_J, m_I\rangle$ basis, with a relative strength determined by ellipticity $\varepsilon(\mathbf{r})$ (Eq. (A2)).

can be written at the corresponding electronic levels in the $|J, I, m_J, m_I\rangle$ basis (referred to as $|m_J, m_I\rangle$ basis in the following), as depicted in Fig. 8b. Furthermore, by choosing a local quantization axis along the helicity axis of the elliptical field \mathbf{e}_h (Eq. (A1)), as those in Fig. 6, then the σ^{\pm} couplings induced by the transverse fields are decoupled. For the general $\mathbf{E}(\mathbf{r})$ in the HE_{11} mode as by Eq. (B1) with local ellipticity $\varepsilon(\mathbf{r}) = \cos(\theta(\mathbf{r}))$, the Rabi coupling strengths are therefore given by Eq (A2) with $\theta \rightarrow \theta(\mathbf{r})$ replaced by the local ellipticity parameter.

While the $|m_J, m_I\rangle$ basis is preferred for understanding the picosecond excitation, a projection back to the atomic hyperfine $|J, I, F, m_F\rangle$ basis (referred to as $|F, m_F\rangle$ in the following) is required to describe any long-time effects. Based on conservation of the magnetic quantum number m_F along the same \mathbf{e}_h axis, the change of basis on the D1 manifold is particularly simple: The “stretched” $|F = I + 1/2, m_F = \pm(I + 1/2)\rangle$ basis are identical to $|m_J = \pm 1/2, m_I = \pm I/2\rangle$. For two-level subspace with smaller $|m_F|$, the matrix $S = (1, 1; -1, 1)/\sqrt{2}$ transforms the $|\pm 1/2, m_F \mp 1/2\rangle$ basis with the $|F \pm 1/2, m_F\rangle$ basis. In particular, for linearly polarized field with $\varepsilon(\mathbf{r}) = 0$, efficient $|g\rangle - |a\rangle$ 2-level dynamics is understood in the local $|m_J, m_I\rangle$ basis as degenerate, independent 2-level controls. At circular polarization $\varepsilon(\mathbf{r}) = 1$, the control field only addresses a particular superposition of $|g\rangle, |d\rangle$ levels (albeit with a strength increased by $\sqrt{2}$). For the more general elliptically polarized HE_{11} field, high quality control can be achieved in the short τ_c limit by improving the control tolerance to the deviation of coupling

strength between Ω_c^{\pm} with composite pulses. These expected control effects at the short τ_c limit are identical to the $I = 0$ case illustrated in Fig. 6. On the other hand, beyond the short τ_c limit, particularly when the local control field is substantial elliptical, more complex strategies have to be developed for achieving precise and robust multi-level controls on the hyperfine manifold [36].

4. Effective D2 linear response

So far in this Appendix, we have outlined a general framework to describe picosecond near-field light-atom interaction on the D1 line. Similar framework is available for the D2 line, and further to include longer interaction time with either stochastic wavefunction methods [72–74] or optical Bloch equations [15, 75].

Here, to support the analysis of the control-probe experiment, we simplify the analysis by perturbatively evaluating the D2 optical response probed by a weak Ω_p pulse through the same ONF interface. Similar to Eq. (C1), we consider the probe pulse with a near-field profile $\mathbf{E}_p(\mathbf{r}, t) = \mathbf{E}(\mathbf{r})S_p(t)$. The spatial profile $\mathbf{E}(\mathbf{r})$ is again evaluated according to Eq. (B1), but at an orthogonal incident polarization according to the Fig. 1a setup ($\Theta \rightarrow \Theta + \pi$). The nanosecond temporal profile, as in Fig. 3, is described by $S_p(t)$ with $|S_p(t)| \leq 1$.

We come to Fig. 8a to understand the nanosecond D2 light-atom interaction in the $|F, m_F\rangle$ basis. For a ground state atom at location \mathbf{r} in the near field, in a general superposition of $|g_m\rangle$ states, the probability of single-photon absorption by the weak $\mathbf{E}_p(\mathbf{r}, t)$ illumination is evaluated perturbatively as

$$\delta\rho_{ee} = \sum_{mm'} \rho_{gmg_{m'}} f_{gmg_{m'}}^e, \quad (\text{C8})$$

with

$$f_{gmg_{m'}}^e(\mathbf{r}) = |\Omega_p^{\text{max}} S_p(\omega_{eg})|^2 \sum_{e,n,l,l'} \mathcal{E}_l^*(\mathbf{r}) \mathcal{E}_{l'}(\mathbf{r}) \mathcal{C}_{e_n g_m}^l \mathcal{C}_{e_n g_{m'}}^{l'}. \quad (\text{C9})$$

Here we define $\mathbf{E}_{\text{max}} = \mathbf{E}(x=0, y=0)$ to be the HE_{11} field strength at the ONF center. The peak reduced Rabi frequency is defined as $\Omega_p^{\text{max}} = |\mathbf{E}_{\text{max}}| |\langle J_g || \mathbf{d} || J_e \rangle| / \hbar$. The normalized field components are defined as

$$\mathcal{E}_l(x, y) = \mathbf{E}(x, y) \cdot \mathbf{e}_l / |\mathbf{E}_{\text{max}}| \quad (\text{C10})$$

for the $l = -1, 0, 1$ local polarizations respectively.

With the probe frequency centered to $\omega_L \approx \omega_{eg}$, the normalized spectrum density for the nanosecond probe to drive the $|g\rangle - |e\rangle$ hyperfine excitation is given by

$$S_p(\omega_{eg}) = \int S_p(t) e^{i(\omega_{eg} - \omega_L)t} dt. \quad (\text{C11})$$

From Eq. (C9) we can derive a single-atom linear attenuation coefficient by comparing the optical energy loss

relative to the incident pulse energy as

$$\begin{aligned}\alpha(\mathbf{r}) &= (\hbar\beta_p \times \delta\rho_{ee}(\mathbf{r})) / \left(\int \varepsilon_0 \mathcal{N}^2 |\mathbf{E}_p(\mathbf{r}, \mathbf{t})|^2 dx dy dt \right) \\ &= \sum_{m,m'} \rho_{g_m g_{m'}} \alpha_{mm'}\end{aligned}\quad (\text{C12})$$

with

$$\alpha_{mm'} = \eta \sum_{e,n,l,l'} \mathcal{C}_{e_n g_m}^l \mathcal{C}_{e_n g_{m'}}^{l'} \mathcal{E}_l^*(x, y) \mathcal{E}_{l'}(x, y) \times \Gamma_e \tau_p. \quad (\text{C13})$$

Here $\Gamma_e \approx 1/26 \text{ ns}^{-1}$ is the D2 natural linewidth. The propagation constant β_p is defined for the HE_{11} mode of the probe pulse. The $\mathcal{N}(x, y)$ describes the index profile of the silica ONF. To arrive at the 2nd line we have assumed short pulses with $\Gamma_e \tau_p \ll 1$ and $\omega_{\text{hfs},e} \tau_p \ll 1$. The η factor for the final $\alpha_m(\mathbf{r})$ expression depends on the ONF geometry and the $S_p(t)$ shape. For the “square pulses” of resonant probe (Fig. 1) and for the silica fiber with $d < \lambda_p$ discussed in this work, the η factor is close to unity.

We now consider that ONF is surrounded by a stationary gas of atoms with a uniform density $\mu(\mathbf{r})$ excluding the ONF core. The initial atomic state is characterized by $\rho^{(0)} = \frac{1}{12}(\mathbf{1}_g + \mathbf{1}_d)$ as those in Eq. (C6) with $\rho_{g_m g_m}^{(0)} = 1/12$. Transmission of the HE_{11} guided probe by the unperturbed gas is $T_0 = e^{-\text{OD}_0}$, with

$$\text{OD}_0 = \int d^3\mathbf{r} \mu(\mathbf{r}) \sum_m \rho_{g_m g_m}^{(0)} \alpha_{mm}(\mathbf{r}). \quad (\text{C14})$$

Immediately after the picosecond control, $\rho_{g_m g_{m'}}(\mathbf{r})$ is modified according to Eq. (D6). The weakly excited D2 atomic dipoles underlying the absorption are reduced in amplitudes and randomized in phases. With in mind the $\Omega_{c,p}$ couplings vary rapidly in the near field, we effectively assume the retained $|g\rangle - |e\rangle$ coherence with random phases contribute negligibly to the optical response afterward. Instead, the absorption is determined by the modified ground state population and coherence as

$$\text{OD} = \int d^3\mathbf{r} \mu(\mathbf{r}) \sum_{m,m'} \rho_{g_m g_{m'}}(\mathbf{r}) \alpha_{mm'}(\mathbf{r}). \quad (\text{C15})$$

The ONF transmission is accordingly enhanced to $T = e^{-\text{OD}}$ at $\Delta t = 0$ control-probe delay. For stationary atoms with $\text{OD} \ll 1$, we expect $\delta\text{OD}/\text{OD}_0$, denoted as $\overline{f_g}$ in the main text for moving atoms, to approximate $\delta\overline{T}$ after a mesoscopic average to be discussed next.

Before proceeding further, we note that optical response of the “stationary gas” prescribed by Eq. (C15) is an effective description of a structure-less homogeneous medium. To arrive at the result, modifications of HE_{11} mode profile by the surrounding atomic gas are ignored. Therefore, the formula can only be applied to a dilute gas. The formalism assists our analysis on the linear optical response of the dilute mesoscopic vapor in the next section, where atomic motion is further taken into account.

The atomic motion in addition helps to effectively smooth out the dipole correlations missed by the single-atom analysis. To investigate the optical response of true “stationary atoms” such as those trapped in a lattice [3, 34], or even just an ensemble of cold atoms [22, 60, 76], more advanced models [15] need to be set up to include near-field dipole-dipole interactions in general.

Appendix D: Mesoscopic average of D2 response

In this section, we derive the optical response of the ONF-atomic vapour system to compare with the experimental measurements. The atomic vapor is assumed to uniformly surround the ONF following a phase-space distribution function

$$g(\mathbf{r}, \mathbf{v}) = \left(\frac{M}{2\pi k_B T} \right)^3 \mu(\mathbf{r}) e^{-M|\mathbf{v}|^2/2k_B T}. \quad (\text{D1})$$

We set $T = 360 \text{ K}$ according to in-vacuum thermometer readout. M is atomic mass of ^{85}Rb and k_B is the Boltzmann constant. The stationary $g(\mathbf{r}, \mathbf{v})$ distribution is assumed to be maintained by a detailed balance of microscopic transportation across the ONF near field. For atoms adsorbed to the ONF surface, we assume an “immediate” desorption, with a new thermal velocity statistically obeying the same Maxwell distribution at T . On the other hand, the internal atomic state is reset to $\rho^{(0)} = \frac{1}{12}(\mathbf{1}_g + \mathbf{1}_d)$ during the surface collision, regardless of the incident state. Finally, we ignore the impact of ONF optical force to $g(\mathbf{r}, \mathbf{v})$.

We label the atoms trespassing the ONF interface according to their initial position and velocity (\mathbf{r}, \mathbf{v}) . For each atom, the temporal forms of the control and probe pulses are modified as $\mathbf{E}_c(\mathbf{r} - \mathbf{v}t, t)$ and $\mathbf{E}_p(\mathbf{r} - \mathbf{v}t, t)$ respectively. Here, for the D1 control we can quite safely ignore the motional broadening since the HE_{11} mode hardly changes over the characteristic nanometer distance $\xi_c = v_T \tau_c$ during the $\tau_c < 100 \text{ ps}$ control. On the other hand, the optical waveform $\mathbf{E}_p(\mathbf{r} - \mathbf{v}t, t)$ can be different substantially from that for stationary atoms, requesting additional evaluations of optical attenuation as those for Eqs. (C14)(C15).

Overall, a straightforward extension of the Appendix C method for the mesoscopic vapor is composed of the following three steps: 1) For atom starting from (\mathbf{r}, \mathbf{v}) with the mixed $\rho^{(0)} = (\mathbf{1}_g + \mathbf{1}_d)/12$ state, evaluating $\rho_{g_m g_{m'}}$ by $U(\mathbf{r})$ for the picosecond control according to Eq. (D6). 2) Evaluating $\alpha_{mm'}(\mathbf{r}, \mathbf{v})$ with the modified $\mathbf{E}_p(\mathbf{r} - \mathbf{v}t, t)$ according to the Appendix C 4 linear analysis. Finally, 3) Performing ensemble average according to the initial $g(\mathbf{r}, \mathbf{v})$ distribution. At $\Delta t = 0$ zero delay (Fig. 3), the probe attenuation in absence from, and in presence of the

control pulse are respectively given by

$$\begin{aligned} \text{OD}_{0,\text{meso}} &= \int d^3\mathbf{r} d^3\mathbf{v} g(\mathbf{r}, \mathbf{v}) \sum_m \rho_{g_m g_m}^{(0)} \alpha_{mm}(\mathbf{r}, \mathbf{v}), \\ \text{OD}_{\text{meso}} &= \int d^3\mathbf{r} d^3\mathbf{v} g(\mathbf{r}, \mathbf{v}) \sum_m \rho_{g_m g_m'} \alpha_{mm'}(\mathbf{r}, \mathbf{v}). \end{aligned} \quad (\text{D2})$$

Even in the linear optics regime, to fully sample $\alpha_{m,m'}(\mathbf{r}, \mathbf{v})$ over the phase-space $g(\mathbf{r}, \mathbf{v})$ distribution by integrating the vectorial light-atom interaction is fairly resource-demanding. In the following we introduce two methods to approximately evaluate OD_{meso} .

1. Monte-Carlo simulation of 2-level atoms

The Monte-Carlo simulation in this work replaces the vectorial light-atom interaction with simple 2-level dynamics [61]. As in Fig. 3c, we consider a cylindrical volume around ONF with a radius of $R = 1 \mu\text{m}$ and a length of $L = 3 \text{ mm}$ to fully cover the near-field interaction zone. Within the volume, we assume a local atomic density $\mu = P/k_B T$ maintained by mesoscopic thermal transportation mentioned earlier with $P \approx 10^{-3}$ pascal. For the Monte Carlo simulation, individual 3-level atoms are initiated at random time to enter the volume through the $r_\perp = R$ surface. The atomic velocity, incident angle, and flux density obey the Maxwell's distribution at $T = 360 \text{ K}$. We choose the simulation time interval of $-t_w/2 < t < t_w/2$, with the control pulse at $0 < t < \tau_c$. A $t_w = 60 \text{ ns}$ time window is chosen for the Monte-Carlo trajectories to reach thermal equilibrium within the cylinder, before the control pulse is fired. The atomic state is initialized as $\rho^0 = |g\rangle\langle g|$. For trajectories hitting the nanofiber surface later, we assume the atom is immediately scattered back to the volume with a new random velocity according to the Maxwell velocity distribution, and with the internal state reset to $|g\rangle$.

We first set the probe pulse with a constant temporal profile to conveniently evaluate the time-dependence of the impact by the control pulse. The photon scattering rate for a moving atom in the near field is evaluated as

$$\gamma(\mathbf{r}, \mathbf{v}, t) = -\frac{1}{\hbar} \text{Im} (E_p^*(\mathbf{r} + \mathbf{v}t) \mathcal{D}_{eg}(t)), \quad (\text{D3})$$

with $\mathcal{D}_{eg}(t) = \rho_{eg}(t) d_{eg}$ to be the expectation value of the electric dipole induced by the weak probe. The coherence $\rho_{eg}(t) = c_g^* c_e$ is evaluated from the atomic state $|\psi(t)\rangle = c_g(t)|g\rangle + c_e(t)|e\rangle + c_a(t)|a\rangle$, which, for most of time, evolves according to the 2-level dynamics

$$\begin{aligned} i\dot{c}_e &= -\frac{i}{2} \Gamma_e c_e + \frac{1}{2} \Omega_p(\mathbf{r} + \mathbf{v}t) c_g, \\ i\dot{c}_g &= \frac{1}{2} \Omega_p^*(\mathbf{r} + \mathbf{v}t) c_e, \end{aligned} \quad (\text{D4})$$

subjected to the Rabi coupling $\Omega_p(\mathbf{r} + \mathbf{v}t) = E_p(\mathbf{r} + \mathbf{v}t) d_{eg}/\hbar$. The non-Hermitian evolution decreases the wavefunction norm $\langle\psi(t)|\psi(t)\rangle$. However, with weak Rabi frequency $\Omega_p \ll 1/\tau_p$ to ensure the linear response,

quantum jumps affects negligibly the interaction dynamics of interest here. We therefore simply renormalize $|\psi(t)\rangle$ after each step of the numerical integration [73, 74].

During $0 < t < \tau_c$, the atomic state is subjected to a $|g\rangle - |a\rangle$ control with the 2-level Rabi frequency $\Omega_c(\mathbf{r} + \mathbf{v}t, t)$ according Eq. (C1). We ignore the probe coupling during the picosecond control. The coherent $|g\rangle - |a\rangle$ dynamics is simply expressed as

$$\begin{aligned} i\dot{c}_a &= \frac{1}{2} \Omega_c(\mathbf{r} + \mathbf{v}t, t) c_g, \\ i\dot{c}_g &= \frac{1}{2} \Omega_c^*(\mathbf{r} + \mathbf{v}t, t) c_a. \end{aligned} \quad (\text{D5})$$

Following the picosecond control, the atomic population is probabilistically projected either to $|g\rangle$ to immediately continue the interaction with the D2 probe according to Eq. (D4), or to $|a\rangle$ where a decay to $|g\rangle$ occurs later via a numerically triggered quantum jump [73, 74] according to the D1 linewidth Γ_a , after a free-flight in dark.

Overall, the ensemble-averaged probe beam scattering rate is written as

$$\gamma_{\text{meso}}(t) = \int d^3\mathbf{r} d^3\mathbf{v} g(\mathbf{r}, \mathbf{v}) \gamma(\mathbf{r}, \mathbf{v}, t). \quad (\text{D6})$$

Numerically, $\gamma_{\text{meso}}(t)$ is simulated with $N_{\text{MC}} = 10^6$ trajectories. To retrieve $\text{OD}_{0,\text{meso}}$ and OD_{meso} for the $\tau_p = 2 \text{ ns}$ probe pulse at various Δt delay as those for Fig. 3 in the main text, we simply convolve $\gamma_{\text{meso}}(t)$ with $S_p(t + \Delta t)$, and normalize the results with the $\hbar\beta_p / \int \varepsilon_0 \mathcal{N}^2 |\mathbf{E}_p(\mathbf{r}, \mathbf{t})|^2 dx dy dt$ factor, similar to Eq. (C9).

The 2-level Monte-Carlo method presented in this section is applied to investigate the time-dependent control-probe dynamics. After the control pulse, the recovery of steady-state probe absorption is decided by the refilling of ground state atoms into the ONF near-field region from two channels: Those desorbed from the ONF surface, and those thermally transported from far away. Within the assumption that atoms desorbed from the ONF wall are in their ground states, the time-dependence in the first channel is hardly affected by the 2-level approximation. For the second channel, the ‘‘refilling time constant’’ is decided by the evanescent control strength $\Omega_c(\mathbf{r})$. For strong enough control, an illumination distance ξ_s is defined within which all the atoms are saturated by the picosecond control. Obviously, ξ_s increase logarithmically with the pulse energy \mathcal{E} . But we note the $g - a$ coupling strength takes the $\Omega_c(\mathbf{r})$ value only for linearly polarized fields. For more general ellipticity the strength is distributed between the σ^\pm couplings as described by Eq. (A2). The distribution of interaction strengths is expected to complicate the recovery dynamics associated with transportation of elliptically excited atoms from far away, beyond the 2-level model. The picture is complicated further by surface interaction [59, 60] and light induced desorption dynamics [62]. All these additional effects may have contributed to the subtle deviation of the theoretical curve in Fig. 3 from experimental measurements in the main text.

2. Convolution of stationary response

We rewrite Eq. (C13) as $\alpha_{mm'}(\mathbf{r}) = \gamma_{mm'}(\mathbf{r})\tau_p$. For an atom traveling at velocity \mathbf{v} , we assume the photon scattering probability is a simple integration of the scattering rate across the free-flight trajectory, so that

$$\alpha_{mm'}(\mathbf{r}, \mathbf{v}) \approx \int_0^{\tau_p} \gamma_{mm'}(\mathbf{r} + \mathbf{v}t) dt. \quad (\text{D7})$$

Ensemble of $\alpha_{mm'}(\mathbf{r}, \mathbf{v})$ are averaged over the Maxwell's velocity distribution to obtain an effective local response $\overline{\alpha_{mm'}}(\mathbf{r})$, which is further simplified as

$$\overline{\alpha_{mm'}}(\mathbf{r}) \approx \int d^3\xi \left(\sqrt{\frac{1}{\xi_p^2 \pi}} \right)^3 e^{-\xi^2/\xi_p^2} \alpha_{mm'}(\mathbf{r} - \xi). \quad (\text{D8})$$

Here $\xi_p = v_T \tau_p / 2$ is the mean thermal diffusion length of the atomic gas during the τ_p flight, $v_T = \sqrt{8k_B T / \pi m}$ is the average thermal velocity. Instead of directly applying ξ_p , we find $\xi'_p = 1.05\xi_p$ more accurately reproduce results from a full-level Monte Carlo simulation [61].

Putting Eq. (D7) into Eq. (D2) and following the Eq. (D8) approximation, we obtain

$$\begin{aligned} \text{OD}_{0,\text{meso}} &\approx \int d^3\mathbf{r} \mu(\mathbf{r}) \sum_m \rho_{gmgm}^{(0)} \overline{\alpha_{mm}}(\mathbf{r}), \\ \text{OD}_{\text{meso}} &\approx \int d^3\mathbf{r} \mu(\mathbf{r}) \sum_{m,m'} \rho_{gmgm'}(\mathbf{r}) \overline{\alpha_{mm'}}(\mathbf{r}). \end{aligned} \quad (\text{D9})$$

Finally, to account for atomic collisions at the ONF surface, during the Eq. (D7) average we simply set $\alpha_{mm'}(\mathbf{r}) = 0$ for $r_\perp < d/2$. Physically, the approximation amounts to that the colliding atoms stick to the wall. The “stick model” generates essentially identical $\overline{\delta T} \approx \delta \text{OD}_{\text{meso}} / \text{OD}_{0,\text{meso}}$ as a more sophisticated model where atoms are immediately desorbed with a re-initialized mixed $\rho^{(0)}$ internal state (as mentioned earlier). This is because the errors associated with the ignored photon-scattering contributions are identical in OD_{meso} and $\text{OD}_{0,\text{meso}}$. The underestimated $\text{OD}_{0,\text{meso}}$ in the “stick model” only affects the $\overline{\delta T}$ estimation by an interaction-independent factor which is effectively compensated for by the atomic density $\mu(\mathbf{r})$ numerically.

Numerically, we follow the Eqs. (D9) (C15) models for the D2 probe linear absorption and the Eqs. (C4)(D6) formalism for the D1 control to evaluate the fractional attenuation $\delta T \approx \bar{f}_g \equiv \delta \text{OD} / \text{OD}_0$, leading to the simulated results in Figs. (4)(5) in the main text.

We finally remark that from Eq. (D2) to Eq. (D9), complex details of coherent atomic dynamics are ignored. The key assumption associated with the approximation is that the photon scattering by atom at any velocity \mathbf{v} and location \mathbf{r} is described by an effective scattering rate, $\gamma(\mathbf{r}) = \sum_{mm'} \gamma_{mm'}(\mathbf{r}) \rho_{gmgm'}(\mathbf{r})$. The “instantaneous following” of stationary optical properties is a justifiable approximation for slowly varying atoms and fields. The same approximation applied to thermal atoms across ONF with the nanosecond transient time could appear

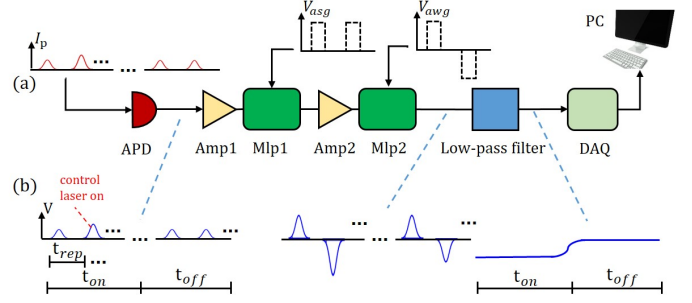


FIG. 9. High speed signal acquisition and averaging. (a): The schematic setup, with the processed signals at each stages represented by the blue curves in (b), from the nanosecond voltage pulse pairs at the APD output, to the slowly varying voltage levels sampled by the DAQ card. The synchronized signals to control the two multipliers (Mlp1 and Mlp2) are generated by an arbitrary sequence generator (CIQTEK ASG8000) and an arbitrary wave generator (CIQTEK AWG4100) respectively. The control pulse is combined with every other probe pulse for $t_{on} = 1.25$ ms and then turned off for $t_{off} = 1.25$ ms for removing the voltage offset.

problematic. However, in the linear optical regime and for thermal atoms uniformly sampling the phase space trajectories, we expect errors associated with the off-diagonal coherent dynamics to average out efficiently toward a “secular approximation” picture. We also expect reduced interaction strength for high speed atoms across the near-field when the transient time is shorter than the probe duration τ_p . However, the spatially uniform coupling strength reduction is largely accounted for by numerically tuning the atomic density in the simulation, not to severely affect the predictions on the control-probe response central to this work. A future step to improve the model is to perform full-level, Monte-Carlo simulation of transient atom-light interaction in the near field including the surface interactions [60].

Appendix E: Experimental Detail

1. High speed signal acquisition and averaging

In the control-probe experiment, we keep the peak power of the nanosecond D2 probe at $P_p \approx 10$ nW level to avoid saturating the atomic absorption. The signal is close to the noise-equivalent power of the 1 GHz avalanche photodiode (APD) module (Hamamatsu C5658). Fortunately, taking advantage of rapid measurement repetition at 4 MHz, enabled by the rapid recovery of the ONF-vapor system (Fig. 3), it is still possible to retrieve fractional change δT with 1% sensitivity within seconds, by rapidly averaging differential absorption. For the purpose, we use off-the-shelf rf components to develop a signal averager schematically illustrated in Fig. 9.

Specifically, the $\tau_p = 2$ ns probe pulse is sent to probe the ONF system with a $t_{rep} = 250$ ns repetition time.

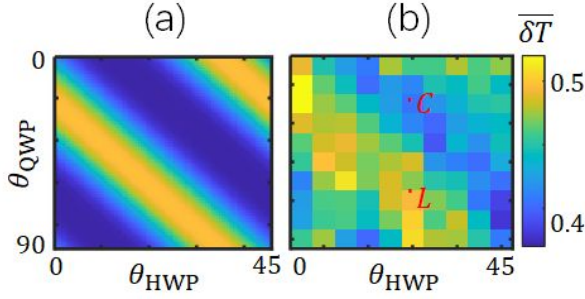


FIG. 10. Simulated (a) and experimentally measured (b) $\overline{\delta T}$ at $\mathcal{E}_1 = 0.2$ pJ, when the polarization states of the orthogonally polarized control and probe pulses (Fig. 1a) are scanned by the HWP and QWP plates before they are coupled to the HE_{11} mode of ONF. Two angular combinations for realizing linear and circular polarized HE_{11} modes are marked with “C” and “L” in the experimental data graph in (b).

A synchronized control pulse is fired immediately before every other probe pulse to form a δT measurement cycle with the nanosecond pulse pairs. As outlined in Fig. 9, after the APD module receive the pulse pairs, they are amplified (Mini-Circuits ZFL-500+) and subjected to two multipliers (AD834) for time-domain filtering and selected pulse sign reversal. The processed signals are then averaged by a 10 kHz bandwidth low-pass filter. The integrated signal level δV reflects the difference of nanosecond probe transmission induced by the picosecond control. The alternating measurement and calibration cycles ensures any slowly varying electronic offset is removed. To compare δV with the probe signal level itself, we remove the second pulse of the probe pulse pair during a $t_0 = 20$ ms interval of $t_{\text{int}} = 200$ ms integration cycle to record V_0 . The low-passed signal is send to computer through a data acquisition (DAQ) card (NI USB-6363). With this method, we integrate 10^7 differential measurements within 3 seconds to obtain $\delta T = \delta V/V_0$ with 1% sensitivity.

2. HE_{11} mode polarization control and measurement

We use a pair of automated half-wave plate (HWP) and quarter-wave plate (QWP) in front of the nanofiber coupler (Figs. 1) to control the polarization states of the HE_{11} mode, for the orthogonally polarized control and probe pulses. An example polarization-dependent $\overline{\delta T}$ measurement with a 2D polarization scan is shown in Fig. 10. As suggested by Fig. 4 of the main text and according to the numerical simulations, the polarization dependence of the transient probe transmission is most pronounced with single control pulses near $\mathcal{E}_1 \sim 0.2$ pJ, which is also the pulse energy value set in this measurement. Representative waveplate angular combinations

with $\varepsilon_{\text{in}} = 0$ and $\varepsilon_{\text{in}} = 1$ are marked with “L” and “C” respectively. The angular combinations are sampled in picosecond controls with single and composite pulses as those in Fig. 4 and Fig. 5.

3. Control and measurement parameter calibration

To interpret experimental measurements as those in Figs. 3 4 5, we need to estimate individual pulse energy \mathcal{E}_j and the peak Rabi frequency Ω_j for the composite pulses. In addition, the steady state ONF attenuation $\Delta T \approx 10\% \sim 20\%$ is measured in between hour-long experiments with moderate accuracy. Drifts of ΔT even at (absolute) 1% level are expected to impact the accuracy of $\overline{\delta T} \equiv \delta T/\Delta T$. The calibrations of these control and measurement parameters are thus required, which are based on a combination of auxiliary measurements and numerical modeling, described in the following.

As mentioned in Sec. III A, the output of the pulse sequence generator is repetition-rate-prescaled and pulse-picked, resulting in a reduced repetition rate of $f'_{\text{rep}} = 4$ MHz that decides the ONF control-probe measurement cycle time t_{rep} . Before the pulses are coupled to ONF, we measure the incident power P with a calibrated power meter (Thorlabs PM160). Taking into account the pre-calibrated fiber coupling efficiency $\eta_C \approx 50\%$, the pulse energy \mathcal{E}_j is estimated as $\mathcal{E}_j = \eta_C t_{\text{rep}} P/N$ for the equal-amplitude N -pulse sequence. Automatic adjustments of the pulse energy is then achieved by scanning the rf signal amplitudes A_j^c in the pulse generation system, which are pre-calibrated to the output pulse power. In particular, the energy of weak pulses follows $\mathcal{E}_j \propto (A_j^c)^4$ in the linear region of AOM operation according to Eq. (1).

We define Ω_j as the peak Rabi frequency of the picosecond pulse at the nanofiber surface average over the angular direction ϕ , $\Omega_j \equiv A_j \langle (\Omega_c(\mathbf{r}))_{r=d/2} \rangle_\phi$, which can be estimated according to Eqs. (C1)(A4) with $\mathbf{E}_c(\mathbf{r}, t)$ inferred from the pulse energy measurements according to the field intensity relation,

$$\frac{1}{2} \int \varepsilon_0 c k_0 \mathcal{N}^2 |\mathbf{E}_c(\mathbf{r}, \mathbf{t})|^2 / \beta_c dx dy dt = N \mathcal{E}_j. \quad (\text{E1})$$

With the experimentally estimated Ω_j , we are able to simulate ONF interface D1 atomic state control and D2 probe dynamics according to the Appendix B C1 C4 methods. The predicted $\overline{\delta f_g}$ are compared with the $\overline{\delta T}$ measurements as those in Figs. 3 4 5 where small discrepancies are usually found. The discrepancies are expected, considering the level of accuracy in the aforementioned estimation. However, simply by uniformly rescaling all the \mathcal{E}_j and $\overline{\delta T}$ values in each full experiment, usually by up to 20% and 10% level respectively, we find very good match between the experimental data and the numerical predictions, as those in Figs. 3 4 5. This suggests the unknown “true values” of \mathcal{E}_j and ΔT (for $\overline{\delta T} = \delta T/\Delta T$) are quite stable during the typical hour-long data-taking processes.

-
- [1] D. E. Chang, J. S. Douglas, A. González-Tudela, C.-L. Hung, and H. J. Kimble, Colloquium : Quantum matter built from nanoscopic lattices of atoms and photons, *Rev. Mod. Phys.* **90**, 31002 (2018).
- [2] L. Tong and E. Mazur, Single-mode guiding properties of subwavelength-diameter silica and silicon wire waveguides, *Opt. Express* **12**, 2905 (2004).
- [3] E. Vetsch, D. Reitz, G. Sague, R. Schmidt, S. T. Dawkins, and A. Rauschenbeutel, Optical Interface Created by Laser-Cooled Atoms Trapped in the Evanescent Field Surrounding an Optical Nanofiber, *Phys. Rev. Lett.* **104**, 203603 (2010).
- [4] L. Tong, F. Zi, X. Guo, and J. Lou, Optical microfibers and nanofibers: A tutorial, *Opt. Commun.* **285**, 4641 (2012).
- [5] P. Solano, J. A. Grover, J. E. Hoffman, S. Ravets, F. K. Fatemi, L. A. Orozco, and S. L. Rolston, Chapter Seven - Optical Nanofibers: A New Platform for Quantum Optics, *Adv. At. Mol. Opt. Phys.* **66**, 439–505 (2017).
- [6] K. P. Nayak, M. Sadgrove, R. Yalla, and F. L. Kien, Nanofiber quantum photonics, *J. Opt.* **20**, 073001 (2018).
- [7] P. Solano, F. K. Fatemi, L. A. Orozco, and S. L. Rolston, Super-radiance reveals infinite-range dipole interactions through a nanofiber, *Nat. Commun.* **8**, 1857 (2019).
- [8] N. V. Corzo, J. Raskop, A. Chandra, A. Aveek, A. S. Sheremet, B. Gouraud, and J. Laurat, Waveguide-coupled single collective excitation of atomic arrays, *Nature*, **566**, 359–362 (2019).
- [9] R. Pennetta, Riccardo, M. Blaha, Martin, A. Johnson, D. Lechner, P. Schneeweiss, J. Volz, and A. Rauschenbeutel, Collective radiative dynamics of an ensemble of cold atoms coupled to an optical waveguide, *Phys. Rev. Lett.* **128**, 73601 (2022).
- [10] Y. He, L. Ji, Y. Wang, L. Qiu, J. Zhao, Y. Ma, X. Huang, S. Wu, and D. E. Chang, Geometric control of collective spontaneous emission, *Phys. Rev. Lett.* **125**, 213602 (2020).
- [11] Y. He, L. Ji, Y. Wang, L. Qiu, J. Zhao, Y. Ma, X. Huang, S. Wu, and D. E. Chang, Atomic spin-wave control and spin-dependent kicks with shaped sub-nanosecond pulses, *Phys. Rev. Res.* **2**, 043418 (2020).
- [12] M. O. Scully, Single Photon Subradiance : Quantum Control of Spontaneous Emission and Ultrafast Readout, *Phys. Rev. Lett.* **115**, 243602 (2015).
- [13] S. J. Masson and A. Asenjo-Garcia, Atomic-waveguide quantum electrodynamics, *Phys. Rev. Res.* **2**, 43213 (2020).
- [14] C. Noh and D. G. Angelakis, Quantum simulations and many-body physics with light, *Reports Prog. Phys.* **80**, 016401 (2017).
- [15] A. Asenjo-Garcia, M. Moreno-Cardoner, A. Albrecht, H. Kimble, and D. E. Chang, Exponential Improvement in Photon Storage Fidelities Using Subradiance and “Selective Radiance” in Atomic Arrays, *Phys. Rev. X* **7**, 031024 (2017).
- [16] T. M. Karg, B. Gouraud, P. Treutlein, and K. Hammerer, Remote Hamiltonian interactions mediated by light, *Phys. Rev. A* **99**, 063829 (2019).
- [17] D. F. Kornovan, N. V. Corzo, J. Laurat, and A. S. Sheremet, Extremely subradiant states in a periodic one-dimensional atomic array, *Phys. Rev. A* **100**, 63832 (2019).
- [18] Y. X. Zhang and K. Mølmer, Theory of Subradiant States of a One-Dimensional Two-Level Atom Chain, *Phys. Rev. Lett.* **122**, 203605 (2019).
- [19] Y. X. Zhang, C. Yu and K. Mølmer, Subradiant bound dimer excited states of emitter chains coupled to a one dimensional waveguide, *Phys. Rev. Res.* **2**, 013173 (2020).
- [20] J. Rui, D. Wei, A. Rubio-abadal, S. Hollerith, D. M. Stamper-kurn, C. Gross, and I. Bloch, A subradiant optical mirror formed by a single structured atomic layer, *Nature* **583**, 369 (2020).
- [21] G. Buonaiuto, F. Carollo, B. Olmos, and I. Lesanovsky, Dynamical Phases and Quantum Correlations in an Emitter-Waveguide System with Feedback, *Phys. Rev. Lett.* **127**, 133601 (2021).
- [22] Y. He, Q. Cai, L. Ji, Z. Fang, Y. Wang, L. Qiu, L. Zhou, S. Wu, S. Grava, and D. E. Chang, Unraveling disorder-induced optical dephasing in an atomic ensemble, Preprint at <http://arxiv.org/abs/2101.10779> (2021).
- [23] A. V. Poshakinskiy and A. N. Poddubny, Dimerization of Many-Body Subradiant States in Waveguide Quantum Electrodynamics, *Phys. Rev. Lett.* **127**, 173601 (2021).
- [24] T. P. Harty, D. T. C. Allcock, C. J. Ballance, L. Guidoni, H. A. Janacek, N. M. Linke, D. N. Stacey, and D. M. Lucas, High-Fidelity Preparation , Gates , Memory & Readout of a Trapped-Ion Quantum Bit, *Phys. Rev. Lett.* **113**, 220501 (2014).
- [25] X. Rong, J. Geng, F. Shi, Y. Liu, K. Xu, W. Ma, F. Kong, Z. Jiang, Y. Wu, and J. Du, Experimental fault-tolerant universal quantum gates with solid-state spins under ambient conditions, *Nat. Commun.* **6**, 8748 (2015).
- [26] Y. Wang, A. Kumar, T. Y. Wu, and D. S. Weiss, Single-qubit gates based on targeted phase shifts in a 3D neutral atom array, *Science* **352**, 1562 (2016).
- [27] C. Sheng, X. He, P. Xu, R. Guo, K. Wang, Z. Xiong, M. Liu, J. Wang, and M. Zhan, High-Fidelity Single-Qubit Gates on Neutral Atoms in a Two-Dimensional Magic-Intensity Optical Dipole Trap Array, *Phys. Rev. Lett.* **121**, 240501 (2018).
- [28] J. Benhelm, G. Kirchmair, C. F. Roos, and R. Blatt, Towards fault-tolerant quantum computing with trapped ions, *Nature Phys.* **4** 463–466 (2008).
- [29] H. Levine, A. Keesling, A. Omran, Ahmed, H. Bernien, S. Schwartz, Sylvain, A. S. Zibrov, M. Endres, M. Greiner, V. Vuletić, and M. D. Lukin, High-Fidelity Control and Entanglement of Rydberg-Atom Qubits, *Phys. Rev. Lett.* **121**, 123603 (2018).
- [30] C. Flühmann, T. L. Nguyen, and M. Marinelli, V. Negnevitsky, K. Mehta, and J. P. Home, Encoding a qubit in a trapped-ion mechanical oscillator, *Nature* **566**, 513 (2019).
- [31] G. T. Genov, D. Schraft, T. Halfmann, and N. V. Vitanov, Correction of Arbitrary Field Errors in Population Inversion of Quantum Systems by Universal Composite Pulses, *Phys. Rev. Lett.* **113**, 043001 (2014).
- [32] G. H. Low, T. J. Yoder and I. L. Chuang, Methodology of resonant equiangular composite quantum gates, *Phys. Rev. X* **6**, 041067 (2016).
- [33] Y. Ma, X. Huang, X. Wang, L. Ji, Y. He, L. Qiu, J. Zhao, Y. Wang, and S. Wu, Precise pulse shaping for quantum control of strong optical transitions, *Opt. Express* **28**,

- 17171 (2020).
- [34] D. Su, R. Liu, Z. Ji, X. Qi, Z. Song, Y. Zhao, L. Xiao, and S. Jia, Observation of ladder-type electromagnetically induced transparency with atomic optical lattices near a nanofiber, *New J. Phys.* **21**, 043053 (2019).
 - [35] W. C. Campbell, J. Mizrahi, Q. Quraishi, C. Senko, D. Hayes, D. Hucul, D. N. Matsukevich, P. Maunz, and C. Monroe, Ultrafast Gates for Single Atomic Qubits, *Phys. Rev. Lett.* **105**, 090502 (2010).
 - [36] L. Qiu, L. Ji, J. Hu, Y. He, Y. Wang, and S. Wu, Precise spinor matterwave control with nanosecond adiabatic spin-dependent kicks, *PRX Quantum* **3**, 040301 (2022).
 - [37] X. Long, S. S. Yu, A. M. Jayich, and W. C. Campbell, Suppressed Spontaneous Emission for Coherent Momentum Transfer, *Phys. Rev. Lett.* **123**, 33603 (2019).
 - [38] M. I. Hussain, D. Heinrich, M. Guevara-Bertsch, E. Torrontegui, J. J. García-Ripoll, C. F. Roos, and R. Blatt, Multi-GHz repetition rate, multi-watt average power, ultraviolet laser pulses for fast trapped-ion entanglement operations, *Phys. Rev. Appl.* **15**, 024054 (2020).
 - [39] S. Zhdanovich, E. A. Shapiro, M. J. Shapiro, W. Hepburn, and V. Milner, Population transfer between two quantum states by piecewise chirping of femtosecond pulses: Theory and experiment, *Phys. Rev. Lett.* **100**, 103004 (2008).
 - [40] L. Piatkowski and N. F. V. Hulst, Ultrafast Meets Ultrasmall: Controlling Nanoantennas and Molecules, *ACS Photonics* **3**, 1401 (2016).
 - [41] P. Dombi, Z. Pápa, J. Vogelsang, S. V. Yalunin, M. Sivilis, G. Herink, S. Schäfer, P. Groß, C. Ropers, and C. Lienau, Strong-field nano-optics, *Rev. Mod. Phys.* **92**, 025003 (2020).
 - [42] S. M. Spillane, G. S. Pati, K. Salit, M. Hall, P. Kumar, R. G. Beausoleil, and M. S. Shahriar, Observation of nonlinear optical interactions of ultralow levels of light in a tapered optical nanofiber embedded in a hot rubidium vapor, *Phys. Rev. Lett.* **100**, 233602 (2008).
 - [43] S. M. Hendrickson, M. M. Lai, T. B. Pittman, and J. D. Franson, Observation of two-photon absorption at low power levels using tapered optical fibers in rubidium vapor, *Phys. Rev. Lett.* **105**, 173602 (2010).
 - [44] V. Venkataraman, K. Saha, P. Londero, and A. L. Gaeta, Few-photon all-optical modulation in a photonic band-gap fiber, *Phys. Rev. Lett.* **107**, 193902 (2011).
 - [45] R. Finkelstein, G. Winer, D. Z. Koplovich, O. Arenfrid, T. Hoinkes, G. Guendelman, M. Netser, E. Poem, A. Rauschenbeutel, B. Dayan, and O. Firstenberg, Super-extended nanofiber-guided field for coherent interaction with hot atoms, *Optica* **8**, 208 (2021).
 - [46] P. Lodahl, S. Mahmoodian, S. Stobbe, A. Rauschenbeutel, P. Schneeweiss, Philipp and J. Volz, Review Chiral quantum optics, *Nature* **541**, 473 (2017).
 - [47] R. Jones, G. Buonaiuto, B. Lang, I. Lesanovsky, and B. Olmos, Collectively Enhanced Chiral Photon Emission from an Atomic Array near a Nanofiber, *Phys. Rev. Lett.* **124**, 93601 (2020).
 - [48] F. Sievers, N. Kretschmar, D. R. Fernandes, D. Suchet, M. Rabinovic, M. and S. Wu, C. V. Parker, L. Khaykovich, C. Salomon, and F. Chevy, Simultaneous sub-Doppler laser cooling of fermionic Li 6 and K 40 on the D1 line: Theory and experiment, *Phys. Rev. A* **91**, 023426 (2015).
 - [49] G. D. Bruce, E. Haller, B. Peaudecerf, D. A. Cotta, M. Andia, S. Wu, M. Y. H. Johnson, B. W. Lovett, and S. Kuhr, Sub-Doppler laser cooling of 40K with Raman gray molasses on the line, *J. Phys. B* **50**, 095002 (2017).
 - [50] T. Ichikawa, M. Bando, Y. Kondo and M. Nakahara, Geometric aspects of composite pulses, *Phil. Trans. R. Soc. Lond. A* **370**, 4671–4689 (2012).
 - [51] P. Emplit, J. P. Hamaide, and F. Reynaud, Passive amplitude and phase picosecond pulse shaping, *Opt. Lett.* **17**, 1358–1360 (1992).
 - [52] D. E. Leaird and A. M. Weiner, Femtosecond optical packet generation by a direct space-to-time pulse shaper, *Opt. Lett.* **24**, 853–855 (1999).
 - [53] T. Mansuryan, M. Kalashyan, J. Lhermite, E. Suran, V. Kermene, A. Barthelemy, and F. Louradour, Compact direct space-to-time pulse shaping with a phase-only spatial light modulator, *Opt. Lett.* **36**, 1635–1637 (2011).
 - [54] P. Lazaridis, G. Debarge, and P. Gallion, Time-bandwidth product of chirped sech2 pulses : application to phase- amplitude- factor measurement, *Opt. Lett.* **20**, 1160, (1995).
 - [55] Y. Meng, A. Dareau, P. Schneeweiss and A. Rauschenbeutel, Near-Ground-State Cooling of Atoms Optically Trapped 300 nm Away from a Hot Surface, *Phys. Rev. X* **8**, 31054 (2018).
 - [56] J. B. Béguin, A. P. Burgers, X. Luan, Z. Qin, S. P. Yu, and H. J. Kimble, Advanced apparatus for the integration of nanophotonics and cold atoms, *Optica* **7**, 2334 (2020).
 - [57] W. S. Leong, M. Xin, Z. Chen, S. Chai, Y. Wang, and S. Y. Lan, Large array of Schrödinger cat states facilitated by an optical waveguide, *Nat. Commun.* **11**, 5295 (2020).
 - [58] R. Liu, Y. Ma, L. Ji, L. Qiu, M. Ji, Z. Tao, and S. Wu, Composite acousto-optical modulation, *Opt. Express* **30**, 27780–27793 (2022).
 - [59] T. Peyrot, Y. R. P. Sortais, J. J. Greffet, A. Browaeys, A. Sargsyan, J. Keaveney, I. G. Hughes, and C. S. Adams, Optical Transmission of an Atomic Vapor in the Mesoscopic Regime, *Phys. Rev. Lett.* **122**, 113401 (2019).
 - [60] P. Solano, and J. A. Grover, Y. Xu, J. N. Munday, L. A. Orozco, W. D. Phillips, and S. L. Rolston, Alignment-dependent decay rate of an atomic dipole near an optical nanofiber, *Phys. Rev. A* **99**, 013822 (2019).
 - [61] Similar to the simplified 2-level model, a full-level Monte Carlo method is developed to simulate the transient response. Limited by the computing demand, we sampled several characteristic points and verified the approximation approaches of mesoscopic average in this work. The details and results will be given in a separate publication.
 - [62] L. Torralbo-Campo, G. D. Bruce, G. Smirne, and D. Cassettari, Light-induced atomic desorption in a compact system for ultracold atoms, *Sci. Rep.* **5**, 14729 (2015).
 - [63] W. Happer, Optical Pumping, *Rev. Mod. Phys.* **44**, 169–249 (1972).
 - [64] D. Goswami, Optical pulse shaping approaches to coherent control, *Physics Report* **374**, 385 (2003).
 - [65] M. Wollenhaupt and T. Baumert, Ultrafast laser control of electron dynamics in atoms, molecules and solids, *Faraday Discuss.* **153**, 9–26 (2011).
 - [66] An improved version of pulse shaper is developed with reduced parameter cross-talk to enable picosecond composite control with $N \geq 5$. The results will be given in a separate publication.
 - [67] M. Maiuri, M. Garavelli, and G. Cerullo, Ultrafast spectroscopy: state of the art and open challenges, *J. Am. Chem. Soc.* **9**, 10533 (2019).

- [68] N. Picqué and T. W. Hänsch, Frequency comb spectroscopy, *Nature Photon.* **13** (2019).
- [69] S. Fuchs, R. Bennett, R. V. Krems, and S. Y. Buhmann, Nonadditivity of Optical and Casimir-Polder Potentials, *Phys. Rev. Lett.* **121**, 83603 (2018).
- [70] D. Hümmer, O. Romero-Isart, A. Rauschenbeutel, and P. Schneeweiss, Probing Surface-Bound Atoms with Quantum Nanophotonics, *Phys. Rev. Lett.* **126**, 163601 (2021).
- [71] E. Vetsch, S. T. Dawkins, R. Mitsch, D. Reitz, P. Schneeweiss, and A. Rauschenbeutel, Nanofiber-based optical trapping of cold neutral atoms, *IEEE J. Sel. Top. Quantum Electron.* **18**, 1763–1770 (2012).
- [72] S. J. Masson, I. Ferrier-barbut, L. A. Orozco, A. Browaeys and A. Asenjo-garcia, Many-Body Signatures of Collective Decay in Atomic Chains, *Phys. Rev. Lett.* **125**, 263601 (2020).
- [73] J. Dalibard, Y. Castin, and K. Molmer, Wave-function approach to dissipative processes in quantum optics, *Phys. Rev. Lett.* **68**, 580 (1992).
- [74] H. J. Carmichael, An open systems approach to quantum optics, *Lecture Notes in Physics*, (Springer, Berlin, 1993).
- [75] M. O. Scully and S. Zubairy, *Quantum Optics*, (Cambridge Univ. Press, Cambridge, 1997).
- [76] G. Sagué, E. Vetsch, W. Alt, D. Meschede, and A. Rauschenbeutel, Cold-atom physics using ultra thin optical fibers: Light-induced dipole forces and surface interactions, *Phys. Rev. Lett.* **99**, 163602 (2007).